

Optimized Design of Crumple Zone on Vehicles

Christopher Tagle, Habiba Eldababy, Kenechukwu Ezeifemeelu

Professor Mostafa Mobasher

Department of Engineering, New York University Abu Dhabi

Senior Design Capstone Project II

ENGR-UH 4011

March 25, 2023

Table of Contents

1.	Abstract.....	3
2.	Problem Definition.....	4
2.1	Problem Analysis	4
2.2	Problem Clarification - Black Box Modeling	6
2.3	Problem Statement	8
3.	Conceptualization	9
3.1	Background Research.....	9
3.2	Concept generation with morphological chart	13
3.3	Concept selection with Pugh chart or Decision matrix	13
4.	Modeling, Simulation, and Optimization Plan/ Experimental Plan.....	20
4.1	Description of Baseline Simulations.....	21
4.2	Baseline Simulation Results and Discussion	35
4.3	Proposed Modified Designs	49
4.4	Description of Simulations for Modified Designs	58
4.5	Experimental Testing of Physical Prototypes	59
5.	Final Design Expected.....	60
6.	Budget.....	62
7.	Implementation Details.....	63
7.1	Progress Summary on Proposed Design	63
7.2	Issues Faced During Implementation/Experimentation	63
7.3	Adjustments Made During Design Implementation	69
7.4	Initial Results for Modified Designs	75
8	Ethics	83
9	Impact of Covid-19.....	85
10.	Did the design meet the requirements?.....	85
11.	Project Management	88
12.	References	89
13.	Appendix	92

1. Abstract

High risk car crashes are a leading cause of death for all age groups across the world, making passenger safety upon high-impact collisions a critical issue to address. The crumple zone is the main absorber of energy for frontal collisions, and longitudinal beams inside the crumple zone are one of the most effective components inside the crumple zone due to their high specific energy absorption. This means that the structure absorbs a large amount of energy compared to its mass. Moreover, car emissions are a main contributor to global warming worldwide and reducing emissions through weight reduction of cars is necessary. There is a need to produce lighter cars with the same safety performance, preferably at an affordable price. Thus, innovation of longitudinal beam design is critical to the design of efficient, lightweight, and cost-effective crumple zones.

Our goal is to investigate different loading scenarios, materials, and geometries for crumple zones with the purpose of optimizing performance, weight, and cost. The design will focus on the longitudinal beams in the crumple zones, optimizing their crash mechanism to absorb maximum energy in high-speed crash scenarios and resist deformation in low-risk bumps. The longitudinal beam designs from existing literature have proven honeycomb structures, thin-walled tubes, and foam integration effective structures for absorbing energy. High strength metals such as steel and aluminum both provide efficient energy absorption at different properties of weight, cost, and hardness. Newer composite materials prove effective energy absorbers when compared to their weight, but the higher cost may be a barrier for use.

The criteria of optimization of the longitudinal beams in the crumple zone are good absorption of impact energy, effective passenger protection, and maintenance of light weighting and cost-effectiveness. The beams should also resist deformation in low impact bumps in order to

avoid large deformation of the crumple zone when the passenger risk is low. Industry standards from the Insurance Institute for Highway Safety (IIHS) and also the National Highway Traffic Safety Administration (NHTSA) are used to evaluate the design performance and viability. The beams will be tested via explicit dynamic simulations on ANSYS, and 3D prototypes of the baseline and optimized designs will be created to be tested experimentally and compared as well.

2. Problem Definition

2.1 Problem Analysis

1.1 Who has the problem?

Car manufacturers and car passengers have the problem of high-risk car crashes. In 2018, road traffic injury was the eighth leading cause of death for all age groups globally, surpassing HIV/AIDS, diarrheal diseases, and other causes [1]. Road traffic injuries caused over 1.2 million deaths in 2018 [1]. Though there was a recent dip in road traffic injuries in the past few years due to the COVID-19 pandemic affecting overall mobility [2], it is likely that numbers will return to comparable pre-COVID values. As a result, passenger collision safety is a highly prioritized and pending issue.

Moreover, cars largely contribute to global emissions of carbon dioxide. Car manufacturers have a need to create lighter cars to achieve the environmental demands of reduced emissions. Lighter cars require less fuel, releasing less carbon dioxide and other emissions. Since cars are an essential part of our modern world, weight-reduction to preserve our environment is necessary.

1.2. What does the problem seem to be?

Optimization of the crumple zone in terms of cost of manufacturing, weight for environmental and cost considerations, and safety of passengers. In particular, the environmental consideration involves weight reduction of the car in order to produce less emissions. Since the crumple zone is very important for the safety of the passengers, reducing its weight while still maintaining its energy-absorbing capabilities and cost is an important issue to consider.

1.3. What are the resources?

Components of the crumple zone (longitudinal beams, crash boxes, firewall, honeycomb structures, foams etc.).

1.4. Why does the problem occur?

- *Why is it important to optimize crumple zones?*

The European Commission has set targets in the future for CO₂ emission reduction. A 15% reduction in CO₂ emissions from cars is targeted for 2025 onward and a 37.5% reduction in CO₂ emissions for 2030 onward [3]. As a result, cars need to be lighter to reduce their energy waste and CO₂ emissions. Thus, it is important to explore decreasing the weight of a crumple zone and its components without sacrificing cost and safety.

- *Why is the bumper, crash box, and longitudinal beam components a key point of optimization?*

These components refer to a specific load path resulting from a frontal collision. They are a key point of optimization as this load path accounts for more than 50% of total energy absorption from collisions [4].

- Why are longitudinal beams a primary area of focus in crumple zone optimization?

Bumpers are important for low-speed collisions to reduce the cost of repair, and crash boxes are thin-walled tubes that are created to absorb energy and deform in high-speed collisions [4]. Longitudinal beams are similar to crash boxes; however, they are much larger and are able to absorb more energy [4]. Thus, in the interest of decreasing weight and increasing energy absorption, crumple zone optimization is primarily focused on longitudinal beams.

1.5. How does the problem occur?

In the interest of sustainability and environmental protection, governments have created targets for decreased CO₂ emissions from cars. This has pushed car manufacturers to find innovative ways to create more innovative and lighter, yet still efficient and safe, car designs.

2.2 Problem Clarification - Black Box Modeling

The below black box model in Figure 1 represents the energy transformation due to the crash where elastic deformation of the car chassis is transformed into plastic deformation of the crumple zone components, friction and heat, and fractures that happen due to reaching the failure point.

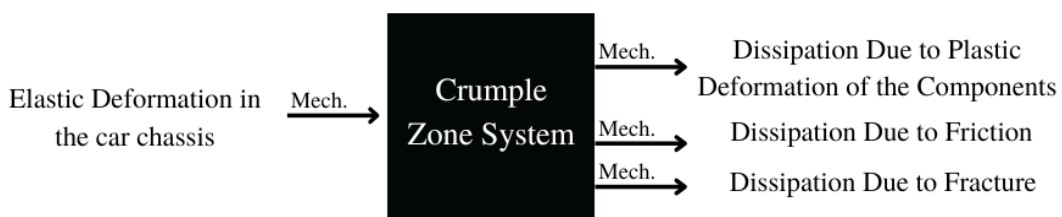


Figure 1. Black box model for the transformation of energy in the crumple zone system

The impact of the car will introduce mechanical energy to the bumper of the car which is the first point of contact between the car and the impact object. The mechanical energy then flows to the crash boxes which are depicted in Figure 2 below. Next, the mechanical energy flows to the firewall and then the longitudinal beams which absorb a large amount of the energy. Finally, it reaches the passenger box where the passenger is inside, and the energy reaching the occupant has been significantly reduced by the previous energy-absorbing components.

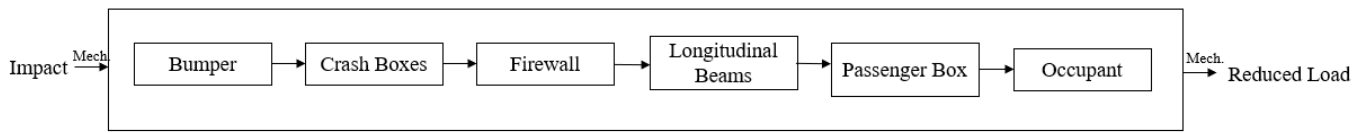


Figure 2. Transmission of energy through the most energy absorbing load path of the crumple zone

zone

Moreover, the longitudinal beam design considers the optimal tube material choice, longitudinal beam shape, and longitudinal beam filling in order to have high energy absorption, low cost, light weight, and low passenger box intrusion. The resulting design is optimized in terms of safety, cost, and weight as seen in Figure 3.



Figure 3. Longitudinal beam design component

2.3 Problem Statement

Crumple zones are one of the major safety features in vehicles, including automobiles and railway vehicles. The crumple zone dissipates large amounts of energy over a long period of time in order to minimize the force acting on passengers in the event of a crash. The crumple zones also ensure that the passenger zone of the vehicle is not intruded or penetrated during a crash. The energy dissipation happens mainly through the plastic deformation of the structural elements. Over the years, different designs of crumple zones have been established in the automotive industry. However, the global automotive industry is challenged to achieve light weight targets throughout the next decade with an overall goal of reducing CO₂ emissions. Lighter cars would consume less energy and lead to lower emissions. The objective of this project is to investigate the different ways in which more optimized crumple zones can be designed to successfully perform their function while being as light as possible.

Our goal is to investigate different loading scenarios, materials, and geometries for crumple zones with the purpose of optimizing both cost and performance while attempting to create a more optimized design. The design will focus on the longitudinal beams in the crumple zones, optimizing their crash mechanism to absorb maximum energy in high-speed crash scenarios and resist deformation in low-risk bumps. To assess the performance of our design, we will use performance metrics based on current industry standards, primarily from the Insurance Institute for Highway Safety (IIHS) and also the National Highway Traffic Safety Administration (NHTSA). These metrics are detailed in Section 4 of this document. Our project's main focus would be to maximize absorbed energy as well as extend the duration of crash to reduce the force transferred.

3. Conceptualization

3.1 Background Research

In 2018, road traffic injury was the eighth leading cause of death for all age groups globally with over 1.2 million deaths, surpassing HIV/AIDS, diarrheal diseases, and other causes [1]. Though there was a recent dip in road traffic injuries in the past few years due to the COVID-19 pandemic affecting overall mobility [2], it is likely that numbers will return to comparable pre-COVID values. As a result, passenger collision safety is a highly prioritized and pending issue. Research and development of collision safety of passengers centers around the concept of “vehicle crashworthiness”. Vehicle crashworthiness refers to the ability of a vehicle and its restraint systems to reduce passenger injury [10]. It is important to note that this does not refer to collision prevention, such as braking mechanisms. Thus, a vehicle is considered to have a higher crashworthiness if, during a collision, passengers experience reduced forces according to thresholds for injury. These vehicle ratings are sourced from standardized crash tests, such as the IIHS or NCAP crash tests. In order to improve passenger safety/vehicle crashworthiness, manufacturers have designed “crumple zones”: structural safety features with the goal to absorb the kinetic energy of vehicles during crashes which may lower the acceleration [4]. The focus of this capstone will be optimizing the design of longitudinal beams, which is a component of the crumple zone. This will be done by tackling the gaps in longitudinal beam research such as the aggregate effect of changing shape and honeycomb cell dimension and wall thickness on the performance of the beam.

Typically, crumple zones are located in the front of the vehicle and are commonly made of metals or plastics. Crumple zones accomplish this energy absorption through its plastic deformation, explaining its name. The three phases of a massive collision are key in order to

understand the design and complexity of a crumple zone. They are the crash initiation phase, the airbag deployment phase, and the occupant contact phase [4]. The crash initiation phase refers to the time where the airbag sensor records a velocity change above 6 km/h within a short time interval; thus, the crumple zone should be stiff enough that this velocity change occurs. However, its stiffness must be relatively low so that, during the airbag deployment phase and occupant contact phase, the car does not decelerate too quickly, and passengers' injury is mitigated [4]. Furthermore, if a crumple zone deforms too easily, it is possible that deformed components of the crumple zone may intrude into the passenger box. With these considerations, an effective crumple zone can reduce collision fatalities dramatically.

The crumple zone consists of multiple components: the bumper, crash boxes and longitudinal beams. While the engine and firewall (wall between engine room and passenger cabin) absorb energy during collision, in most crashworthiness studies they are considered rigid [4]. The bumper is located at the front of the crumple zone, furthest away from the passenger box, and is usually made of steel, plastic, or composites. It is effective during low-speed crashes, as it decreases the cost of repair. Crash boxes are thin-walled tubes that collapse during collisions in a specific pattern to absorb energy. Longitudinal beams are also thin-walled structures but are larger and usually absorb more energy than crash boxes [4]. Figure 4 shows the different paths that force from a collision will travel through in the front of a vehicle. Path 1, which includes the bumper, crash box, and longitudinal beams, absorbs more than 50% of total energy in most frontal collisions [4].

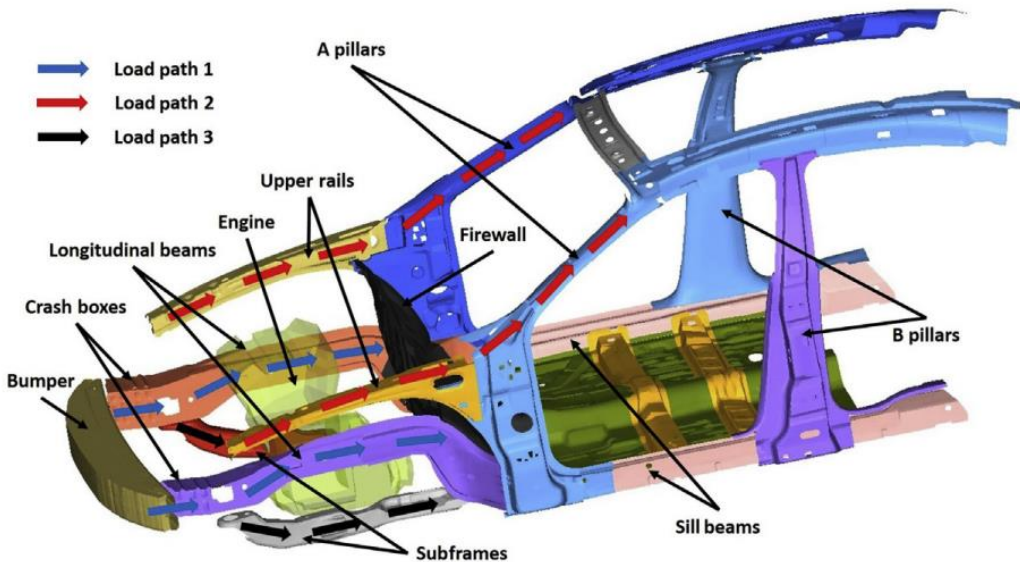


Figure 4. Force Paths of Vehicle Frontal Structure [4]

Because of the orientation of certain components of the crumple zone, during collision, the greatest forces are recorded on longitudinal components [4]. These primarily consist of the crash boxes and the longitudinal beams. As mentioned, longitudinal bars are similar to crash boxes in function, except they are larger and, thus, are able to absorb more energy [4]. As a result, longitudinal beams are arguably the most critical component of an effective crumple zone. This has led to research on longitudinal beam design to be a primary focus in crumple zone optimization.

Research into longitudinal beam optimization has explored various methods to increase energy absorption such as tube shape, foams, honeycomb patterns. For materials, steel is most commonly used due to its ductility and high tensile strength, which allows for it to plastically deform and absorb a significant amount of energy. Steel's accessibility and relatively low price are also reasons for its use. Furthermore, various kinds of filling for the tubular structures have been explored to improve energy absorption. Lightweight materials such as aluminum honeycomb

or foam have been used. Honeycomb-filled tubes are becoming increasingly common in crumple zones due to its high strength to weight ratio [9]. Recent research has begun exploring functionally graded honeycomb patterns in tubes and have found improvements in energy absorption in comparison to uniform thickness honeycombs [11]. These refer to honeycomb patterns with varying wall thickness, where thickness increases towards the corners of each cell. Lastly, past literature also explored foam-filled tubes and foam-and-honeycomb-filled tubes and were found to improve energy absorption [9] in comparison to regular hollow tubes. However, there is a gap in research as the use of functionally graded honeycomb and foam-filled tubes and its feasibility has not been explored. Furthermore, a combination of this design with different longitudinal beam shapes, such as enneagonal (nine-sided), has not been explored, though enneagonal tube shapes have proven to have comparable if not better specific energy absorption than circular tubes [12].

3.2 Concept generation with morphological chart

Table 3: Morphological Chart

Means	Function		
	Optimal Tube Material Choice	Longitudinal Beam Shape	Longitudinal Beam Filling
1	Steel	Circular	Simple aluminum honeycomb filling + Foam (ex: polyurethane foam)
2	Aluminum	Enneagonal (nine-sided polygon)	Functionally graded aluminum honeycomb filling + Foam (ex: polyurethane foam)

3.3 Concept selection with Pugh chart or Decision matrix

Pugh charts are used to evaluate concepts based on some predefined criteria in order to reduce the likelihood of selecting wrong concepts or eliminating promising design concepts. The concepts chosen to be evaluated are derived from the morphological chart in Table 3 and are shown in Table 4 below. In the Pugh charts shown in Table 5-12, one concept is made the base concept and the other concepts are evaluated against it with the following score: 1 (superior), 0 (similar), -1 (inferior). The sum of the scores is used to determine the best design candidates. If the sum for

a concept remains relatively high in all the Pugh chart iterations, that concept is likely to be our project's strongest candidate.

Table 4: Description on the Most Promising Options for the Optimized Design of Crumple Zone on Vehicles.

Concept	Description
1	<u>Optimal Tube Material Choice:</u> Steel <u>Longitudinal Beam Shape:</u> Circular <u>Longitudinal Beam Filling:</u> Simple aluminum honeycomb filling + Foam (ex: polyurethane foam)
2	<u>Optimal Tube Material Choice:</u> Steel <u>Longitudinal Beam Shape:</u> Circular <u>Longitudinal Beam Filling:</u> Functionally graded aluminum honeycomb filling + Foam
3	<u>Optimal Tube Material Choice:</u> Steel <u>Longitudinal Beam Shape:</u> Enneagonal <u>Longitudinal Beam Filling:</u> Simple aluminum honeycomb filling + Foam (ex: polyurethane foam)
4	<u>Optimal Tube Material Choice:</u> Steel <u>Longitudinal Beam Shape:</u> Enneagonal <u>Longitudinal Beam Filling:</u> Functionally graded aluminum honeycomb filling + Foam
5	<u>Optimal Tube Material Choice:</u> Aluminum <u>Longitudinal Beam Shape:</u> Circular <u>Longitudinal Beam Filling:</u> Simple aluminum honeycomb filling + Foam (ex: polyurethane foam)
6	<u>Optimal Tube Material Choice:</u> Aluminum <u>Longitudinal Beam Shape:</u> Circular <u>Longitudinal Beam Filling:</u> Functionally graded aluminum honeycomb filling + Foam
7	<u>Optimal Tube Material Choice:</u> Aluminum <u>Longitudinal Beam Shape:</u> Enneagonal <u>Longitudinal Beam Filling:</u> Simple aluminum honeycomb filling + Foam (ex: polyurethane foam)

8	<u>Optimal Tube Material Choice:</u> Aluminum <u>Longitudinal Beam Shape:</u> Enneagonal <u>Longitudinal Beam Filling:</u> Functionally graded aluminum honeycomb filling + Foam
----------	--

The above concepts were weighed against the following criteria:

- i. **Cost** - Relatively cheap to fabricate models are favored to more expensive ones. It is also important to note that on an industrial level, designs that are originally expensive could have their costs reduced due to economies of large-scale production.
- ii. **Weight** - Lighter models are favored as it reduces the fuel consumption/energy requirement of the vehicle in motion. This also points towards a more sustainable design.
- iii. **Expected Energy Dissipated** - Longitudinal Beam models that dissipate the most energy, reducing the collision's effect on the passengers, are preferred. More information such as exact specific energy absorption values (SEA) would be known after the appropriate simulations have been carried out.
- iv. **Expected Measured Intrusion into Passenger Box** - Longitudinal Beam models that result in the least displacement of car parts into the passenger box are preferred as they reduce the risk of injuries on passengers.

Table 5: Pugh Chart on Optimized Design of Crumple Zone on Vehicles Project - Concept 1

Baseline

Concept	Cost	Weight	Exp. Energy Dissipated	Exp. Measured Intrusion	Sum
1	BASE				
2	-1	0	1	1	1
3	-1	0	1	1	1
4	-1	0	1	1	1
5	1	1	-1	-1	0
6	1	1	-1	-1	0
7	1	1	-1	-1	0
8	1	1	-1	-1	0

Table 6: Pugh Chart on Optimized Design of Crumple Zone on Vehicles Project - Concept 2

Baseline

Concept	Cost	Weight	Exp. Energy Dissipated	Exp. Measured Intrusion	Sum
1	1	0	-1	-1	-1
2	BASE				
3	0	0	0	0	0
4	-1	0	1	1	1
5	1	1	-1	-1	0
6	1	1	-1	-1	0
7	1	1	-1	-1	0
8	1	1	-1	-1	0

Table 7: Pugh Chart on Optimized Design of Crumple Zone on Vehicles Project - Concept 3

Baseline

Concept	Cost	Weight	Exp. Energy Dissipated	Exp. Measured Intrusion	Sum
1	1	0	-1	-1	-1
2	0	0	0	0	0
3	BASE				
4	-1	0	1	1	1
5	1	1	-1	-1	0
6	1	1	-1	-1	0
7	1	1	-1	-1	0
8	1	1	-1	-1	0

Table 8: Pugh Chart on Optimized Design of Crumple Zone on Vehicles Project - Concept 4

Baseline

Concept	Cost	Weight	Exp. Energy Dissipated	Exp. Measured Intrusion	Sum
1	1	0	-1	-1	-1
2	1	0	-1	-1	-1
3	1	0	-1	-1	-1
4	BASE				
5	1	1	-1	-1	0
6	1	1	-1	-1	0
7	1	1	-1	-1	0
8	1	1	-1	-1	0

Table 9: Pugh Chart on Optimized Design of Crumple Zone on Vehicles Project - Concept 5

Baseline

Concept	Cost	Weight	Exp. Energy Dissipated	Exp. Measured Intrusion	Sum
1	-1	-1	1	1	0
2	-1	-1	1	1	0
3	-1	-1	1	1	0
4	-1	-1	1	1	0
5	BASE				
6	-1	0	1	1	1
7	-1	0	1	1	1
8	-1	0	1	1	1

Table 10: Pugh Chart on Optimized Design of Crumple Zone on Vehicles Project - Concept 6

Baseline

Concept	Cost	Weight	Exp. Energy Dissipated	Exp. Measured Intrusion	Sum
1	-1	-1	1	1	0
2	-1	-1	1	1	0
3	-1	-1	1	1	0
4	-1	-1	1	1	0
5	1	0	-1	-1	-1
6	BASE				
7	0	0	0	0	0
8	-1	0	1	1	1

Table 11: Pugh Chart on Optimized Design of Crumple Zone on Vehicles Project - Concept 7

Baseline

Concept	Cost	Weight	Exp. Energy Dissipated	Exp. Measured Intrusion	Sum
1	-1	-1	1	1	0
2	-1	-1	1	1	0
3	-1	-1	1	1	0
4	-1	-1	1	1	0
5	1	0	-1	-1	-1
6	0	0	0	0	0
7	BASE				
8	-1	0	1	1	1

Table 12: Pugh Chart on Optimized Design of Crumple Zone on Vehicles Project - Concept 8

Baseline

Concept	Cost	Weight	Exp. Energy Dissipated	Exp. Measured Intrusion	Sum
1	-1	-1	1	1	0
2	-1	-1	1	1	0
3	-1	-1	1	1	0
4	-1	-1	1	1	0
5	1	0	-1	-1	-1
6	1	0	-1	-1	-1
7	1	0	-1	-1	-1
8	BASE				

After the Pugh chart analysis in Table 6-12 above, the total number of times each concept was assigned a sum score has been compiled in Table 13 below.

Table 13: Outcome of Sum Scores from Pugh Chart Analysis

Concept	Number of Times		
	Sum = 1	Sum = 0	Sum = -1
1	----	4	3
2	1	5	1
3	1	5	1
4	3	4	----
5	----	4	3
6	1	5	1
7	1	5	1
8	3	4	----

As seen from Table 13 above, Concepts 4 and 8 prove to be the most promising designs with Concept 1 and 5 emerging as the weakest candidates. As such, Concept 4 and 8 should be further investigated to determine which design is stronger based on the performance criteria.

4. Modeling, Simulation, and Optimization Plan/ Experimental Plan

For modeling and testing, both finite element modeling will be used as well compressive testing of 3D printed specimens. The simulations results will be used more frequently used since it is easier to change the parameters of the design while optimizing it. Furthermore, experimental testing brings issues such as item procurement complications and manufacturing time expenses. Below is a flowchart summary of the testing plan including simulation and experiments. Each stage will be discussed in more detail.

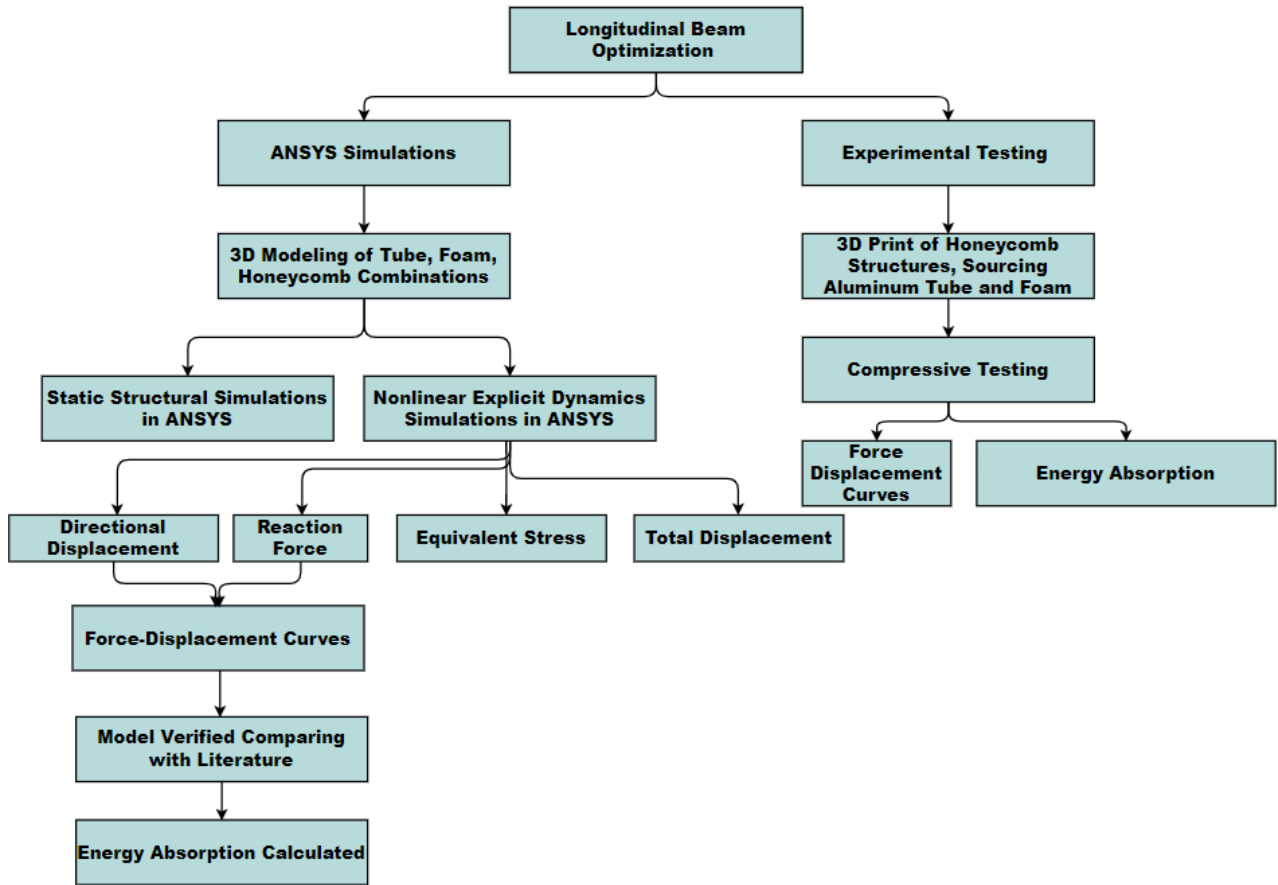


Figure 5. Flowchart Representing the Testing Process

4.1 Description of Baseline Simulations

All models to be simulated consist of at least one of three different components listed below which will be modeled using SOLIDWORKS. The details of their dimensioning and material assignments can be found in Section 5.

1. Aluminum Square Tube (AST)
2. Polyurethane Foam (P)
3. Aluminum Honeycomb Filling (H)

These models will be nonlinear explicit dynamic simulations in ANSYS which will compress the geometry axially to mimic the behavior of a crumple zone during collision. A summary of the simulation process is displayed in the flowchart below in Figure 6.

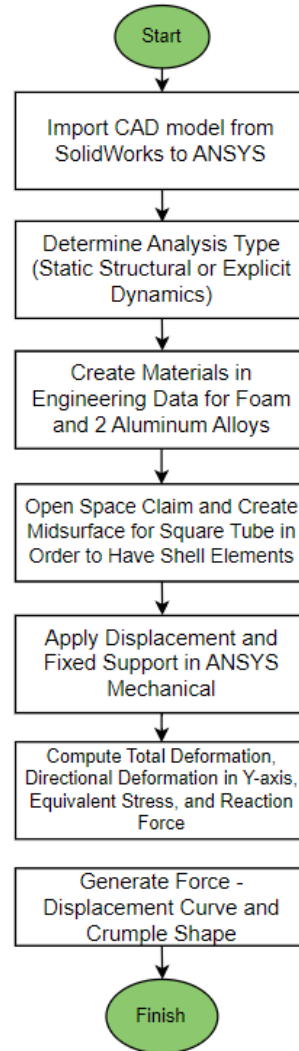


Figure 6. Flowchart Representation of Simulation Process

4.1.1 Elastic-Perfectly Plastic Material Model

The aluminum square tube, aluminum honeycomb filling, and the polyurethane foam will all be treated as elastic-perfectly plastic materials. An elastic-perfectly plastic material refers to a model of a material whose stress-strain curve follows the behavior of Figure 7 (b) [16].

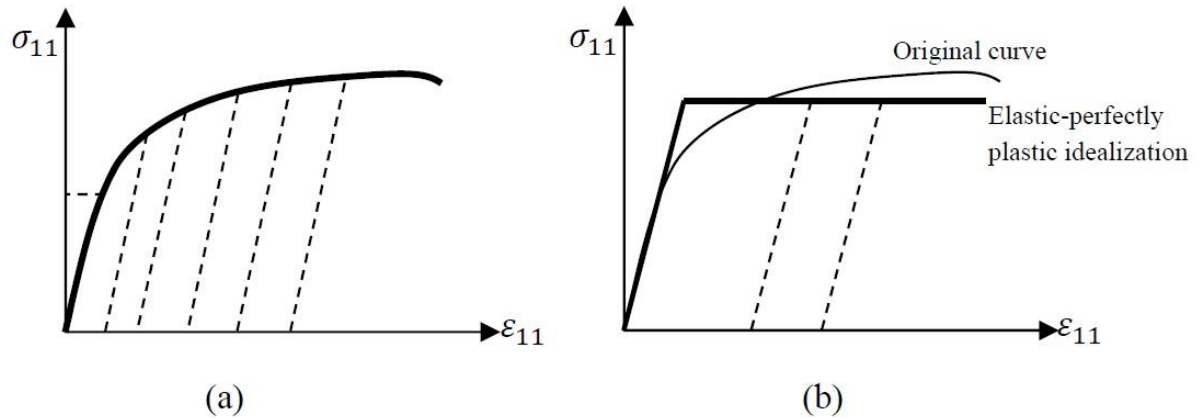


Figure 7. Stress-strain curve of Original Curve Versus Elastic-Perfectly Plastic Model [16]

Essentially, under strain, the material will deform elastically at first, indicated by the linearity of the curve at the beginning of the graph. As the stress increases, the strain also increases linearly and vice versa. However, once the material yields, the material will deform plastically with stress remaining constant as strain increases. Using ANSYS, each individual geometry will be compressed into their elastic and then plastic region, if time allows for the computational load, and their behavior will be compared to the findings from R. D. Hussein et al. [9], where crushing behavior of these individual geometries are described.

Once the individual models are verified, the following assemblies on SOLIDWORKS will be created. The details of their dimensioning and material assignments can be found in Section 5.

1. Aluminum Square Tube filled with Polyurethane Foam (ASTP)
2. Aluminum Square Tube filled with Aluminum Honeycomb Filling (ASTH)
3. Aluminum Square Tube Filled with Polyurethane Foam and Aluminum Honeycomb Filling (ASTHP)

The contact between the geometries will be bonded and a loading within the elastic and then plastic region of the material will be simulated. The results will once again be verified with data from R. D. Hussein et al [9], where crushing behavior of these assemblies are described.

4.1.2 Material Properties of Components

The material properties were assigned to the components as shown in Table 14 below. The foam properties were found by digitizing the graphs from R. D. Hussein et al using the Origin Pro software [9]. The stress-strain curve for the aluminum square tube from R.D Hussein et al. were digitized to find the Young's Modulus and Yield Stress, but due to the steep curve of the graph, the Young's Modulus was difficult to accurately obtain using digitization software such as Origin Pro. Thus, online material specifications from a manufacturer were utilized for the square tube and are shown below [13]. Moreover, the properties for the honeycomb aluminum alloy 5052-H39 were also obtained online where density, Young's modulus, and Poisson's ratio are from [14], and the yield strength is from [15]. Note that tangent modulus was set to 0 for the elastic-perfectly plastic model as seen from the straight horizontal line in Figure 8 below.

Table 14. Material Properties

	Density	Young's Modulus	Poisson Ratio	Yield Strength	Tangent Modulus
Foam (Polyurethane Foam)	180 kg/m ³	67.74 MPa	0.3	2.41909 MPa	0
Tube (Aluminum Alloy AA 6060-T5)	2.70 g/cc	68.9 GPa	0.33	145 MPa	0
Honeycomb (Aluminum 5052-H39)	2.7g/cm ³	68 GPa	0.33	255 MPa	0

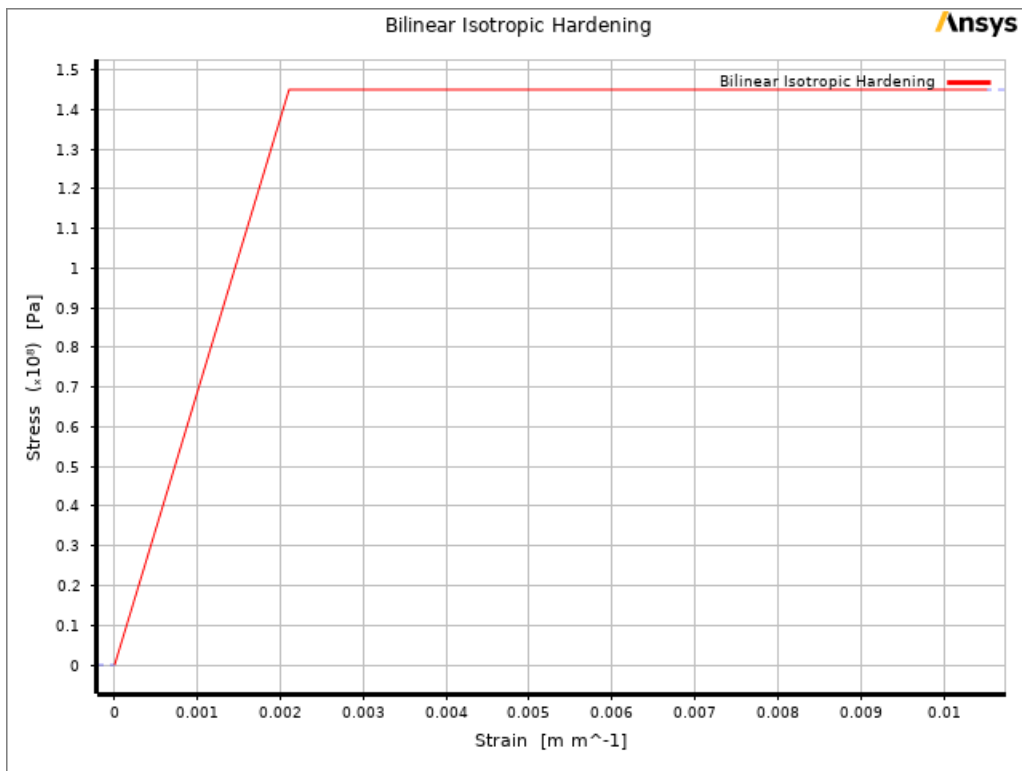


Figure 8. Sample Stress-Strain Plot for Elastic-Perfectly Plastic Model for AA 6060 T-5

4.1.3 Setup for FEA Simulations

4.1.3.1 Geometry and Mesh Element Type

As mentioned in Section 5, SOLIDWORKS models of different longitudinal beam designs will be created and imported into ANSYS. It is important to note that only the foam is modeled as a solid body, while the honeycomb and square tube are modeled as shell elements. This is done by creating a mid-surface on SpaceClaim. If the square tube is being modeled as a shell, then a thickness of 1.5 mm will be assigned. If the honeycomb is being modeled as a shell, then a thickness of 0.0508 mm will be assigned. Shell elements were chosen over solid elements because proper bending for solids can only be properly captured with 4 or more mesh elements across a

thickness. However, this is not practical due to how thin these walls are; thus, shell elements are used instead as they capture bending accurately.

The geometry of each simulation is derived from different combinations of the three individual parts: aluminum square hollow tube, aluminum honeycomb filling and polyurethane foam. These geometries can be seen in Figure 9 below:

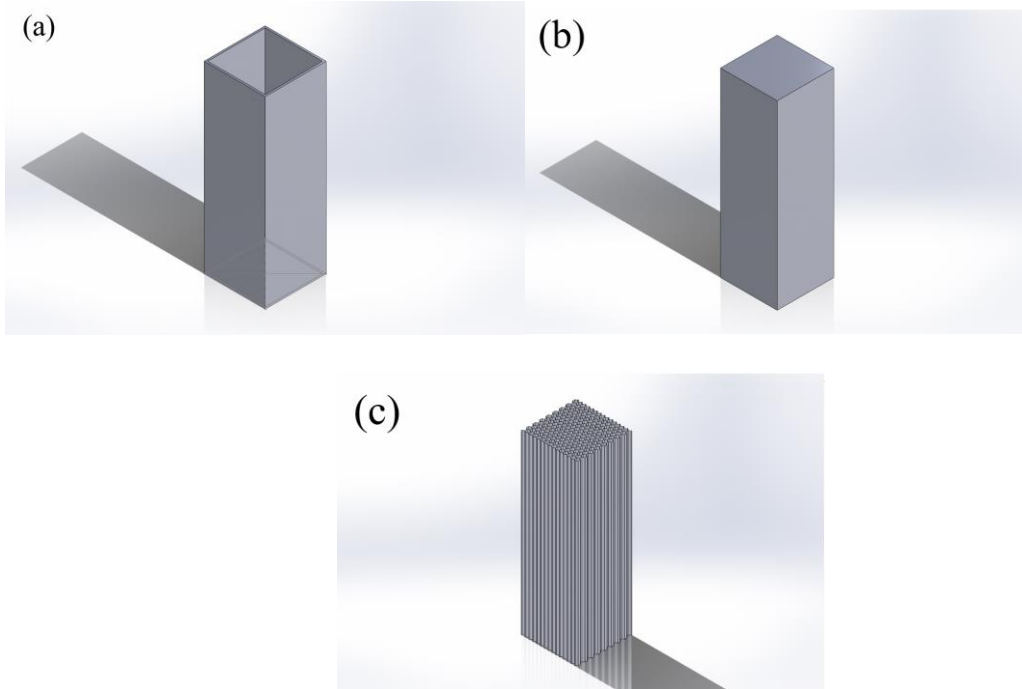


Figure 9. Geometries of Individual Components. (a) Square Hollow Tube (b) Foam (c) Honeycomb

4.1.3.2 Boundary Conditions

In order to mimic the compression of a longitudinal beam during a collision, the following boundary conditions were used. Figure 10a shows an example of the boundary conditions applied to the square tube. First, fixed supports were applied to the bottom face/faces of the structure. An example of the fixed support boundary condition on a hollow square tube is shown in Figure 10a. In other more complicated geometries with multiple components, such as a foam-filled tube or a honeycomb-filled tube, it is important to fix both bottom faces of each component. Then,

displacement boundary conditions were applied to the top face/faces of the structure. An example of the displacement boundary condition of a hollow square tube is shown in Figure 10b.

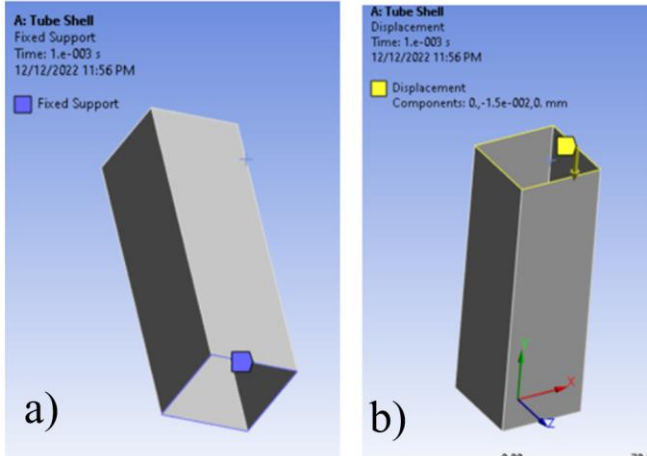


Figure 10. Boundary Conditions as shown on Square Tube (a) Fixed Support (b)

Displacement

The displacement conditions were then applied linearly in a preset number of steps up to a chosen maximum displacement. The maximum displacement and preset number of steps varied based on computational resources and type of experiment. Figure 11 below shows an example of the displacement conditions performed with 10 steps up to a displacement of 0.15 mm.

	Steps	Time [s]	<input checked="" type="checkbox"/> X [mm]	<input checked="" type="checkbox"/> Y [mm]	<input checked="" type="checkbox"/> Z [mm]
1	1	0.	0.	0.	0.
2	1	1.e-003	0.	-1.5e-002	0.
3	2	2.e-003	= 0.	= -3.e-002	= 0.
4	3	3.e-003	= 0.	= -4.5e-002	= 0.
5	4	4.e-003	= 0.	= -6.e-002	= 0.
6	5	5.e-003	= 0.	= -7.5e-002	= 0.
7	6	6.e-003	= 0.	= -9.e-002	= 0.
8	7	7.e-003	= 0.	= -0.105	= 0.
9	8	8.e-003	= 0.	= -0.12	= 0.
10	9	9.e-003	= 0.	= -0.135	= 0.
11	10	1.e-002	= 0.	-0.15	= 0.
*					

Figure 11. Displacement Tabular Data Example Using 10 Time Steps for Maximum 0.15mm

Displacement.

4.1.4 Elastic Model / Model Verification

The model was verified in the elastic region by checking that the following relationships hold in the elastic region. Verification of the model checks that our FEA solutions result in precise answers. On moving into the plastic region, analytical solutions become impractical, hence verification can only be carried out in the linear elastic region. The stiffness value is then calculated as shown below with the FEA and theoretical methods. The stiffness value from the FEA solution is then compared with the stiffness value from the theoretical method.

$$k_{theory} = \frac{EA}{L} \quad k_{FEA} = \frac{F}{x}$$

k = stiffness E = Young's Modulus L = Length

x = deformation F = Reaction Force

Tube Model Verification

The material properties of the tube were taken from Table 14 above. From analytical calculations in the elastic region:

$$k_{theory} = \frac{EA}{L} = \frac{(68.9 \times 10^9 \text{ Pa}) \times (291 \times 10^{-6} \text{ m}^2)}{0.15\text{m}} = 133.667 \times 10^6 \text{ N/m}$$

Deformation at yield (x_y):

$$\sigma_y = E \frac{x_y}{L}; \quad x_y = \frac{\sigma_y}{E} L$$

$$x_y = \frac{145 \text{ MPa}}{68.9 \times 10^3 \text{ MPa}} \times 150\text{mm} = 0.3157\text{mm}$$

Applying a maximum deformation of $x = 0.15$ mm in 10 steps (i.e., a deformation within the elastic region of the model), the reaction force at the top face was determined from the FEA simulation.

$$\text{Reaction Force, } F = 20.273 \text{ kN}$$

Therefore, from FEA simulation:

$$k_{\text{FEA}} = \frac{F}{x} = \frac{20.273 \text{ kN}}{0.15 \times 10^{-3} \text{ m}} = 135.153 \times 10^6 \text{ N/m}$$

Percentage Error:

$$\% \text{ Error} = \left| \frac{k_{\text{FEA}} - k_{\text{theory}}}{k_{\text{theory}}} \right| = \left| \frac{135.153 - 133.667}{133.667} \right| \times 100\% = 1.11\%$$

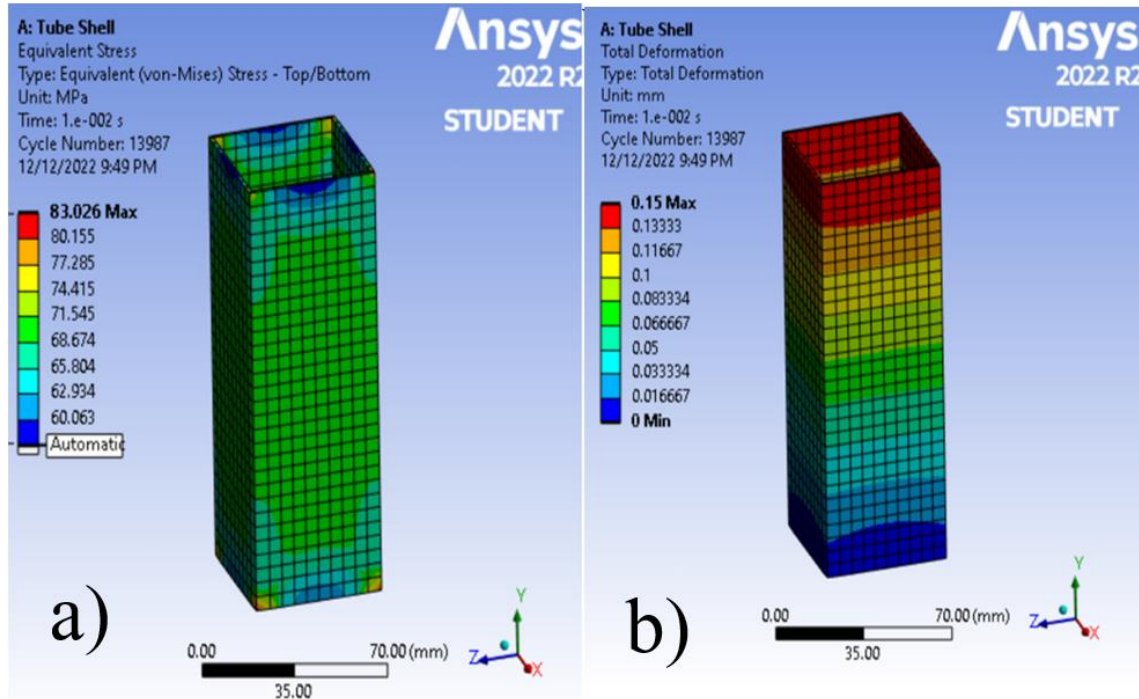


Figure 12. Plot of a) Equivalent (von-Mises) Stress Distribution and b) Total Deformation in Tube for a Deformation of 0.15mm (in the -Y Direction)

Honeycomb Model Verification

The material properties of the honeycomb were taken from Table 14 above. From analytical calculations in the elastic region:

$$k_{\text{theory}} = \frac{EA}{L} = \frac{(68 \times 10^9 \text{ Pa}) \times (69.67 \times 10^{-6} \text{ m}^2)}{0.05 \text{ m}} = 94.7512 \times 10^6 \text{ N/m}$$

Deformation at yield (x_y):

$$\sigma_y = E \frac{x_y}{L}; \quad x_y = \frac{\sigma_y}{E} L$$

$$x_y = \frac{255 \text{ MPa}}{68 \times 10^3 \text{ MPa}} \times 50 \text{ mm} = 0.1875 \text{ mm}$$

Applying a maximum deformation of $x = 0.01 \text{ mm}$ in 10 steps (i.e., a deformation within the elastic region of the model), the reaction force at the top face was determined from the FEA simulation.

Reaction Force, $F = 928.2 \text{ N}$

Therefore, from FEA simulation:

$$k_{\text{FEA}} = \frac{F}{x} = \frac{928.2 \text{ N}}{0.01 \times 10^{-3} \text{ m}} = 92.82 \times 10^6 \text{ N/m}$$

Percentage Error:

$$\% \text{ Error} = \left| \frac{k_{\text{FEA}} - k_{\text{theory}}}{k_{\text{theory}}} \right| = \left| \frac{92.82 - 94.7512}{94.7512} \right| \times 100\% = 2.038\%$$

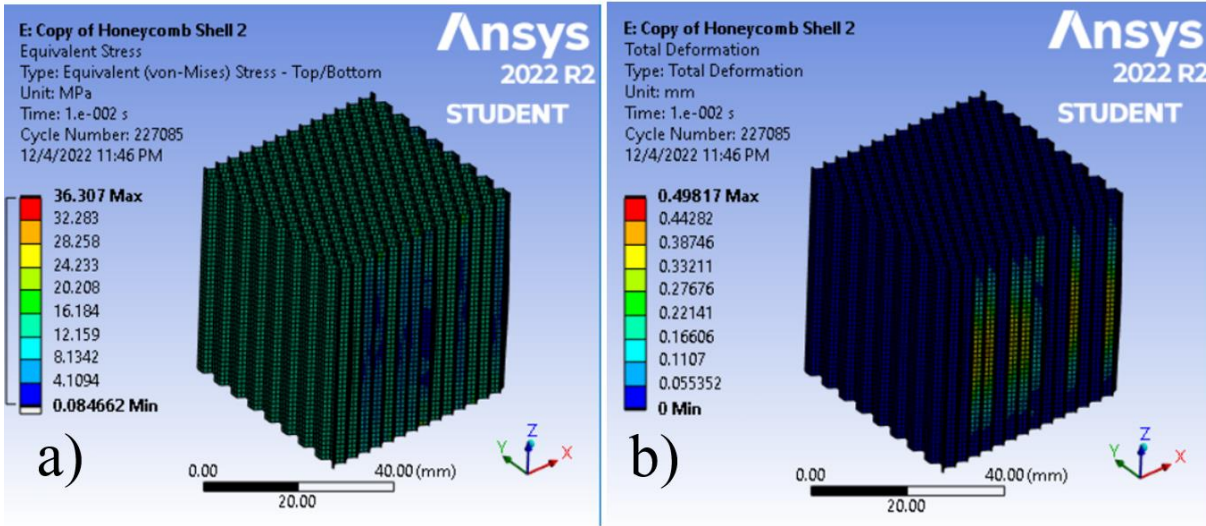


Figure 13. Plot of a) Equivalent (von-Mises) Stress Distribution and b) Total Deformation in Honeycomb for a Deformation of 0.01mm (in the -Z Direction)

Foam Model Verification

The material properties of the foam were taken from Table 14 above. From analytical calculations in the elastic region:

From analytical calculations:

$$k_{\text{theory}} = \frac{EA}{L} = \frac{(67.74 \times 10^6 \text{ Pa}) \times (2209 \times 10^{-6} \text{ m}^2)}{0.05 \text{ m}} = 2.993 \times 10^6 \text{ N/m}$$

Deformation at yield (x_y):

$$\sigma_y = E \frac{x_y}{L}; \quad x_y = \frac{\sigma_y}{E} L$$

$$x_y = \frac{2.41909 \text{ MPa}}{67.74 \text{ MPa}} \times 50 \text{ mm} = 1.786 \text{ mm}$$

Applying a maximum deformation of $x = 0.5$ mm in 10 steps (i.e., a deformation within the elastic region of the model), the reaction force at the top face was determined from the FEA simulation.

$$\text{Reaction Force, } F = 1600 \text{ N}$$

Therefore, from FEA simulation:

$$k_{\text{FEA}} = \frac{F}{x} = \frac{1600 \text{ N}}{0.5 \times 10^{-3} \text{ m}} = 3.2 \times 10^6 \text{ N/m}$$

Percentage Error:

$$\% \text{ Error} = \left| \frac{k_{\text{FEA}} - k_{\text{theory}}}{k_{\text{theory}}} \right| = \left| \frac{3.2 - 2.993}{3.2} \right| \times 100\% = 6.469\%$$

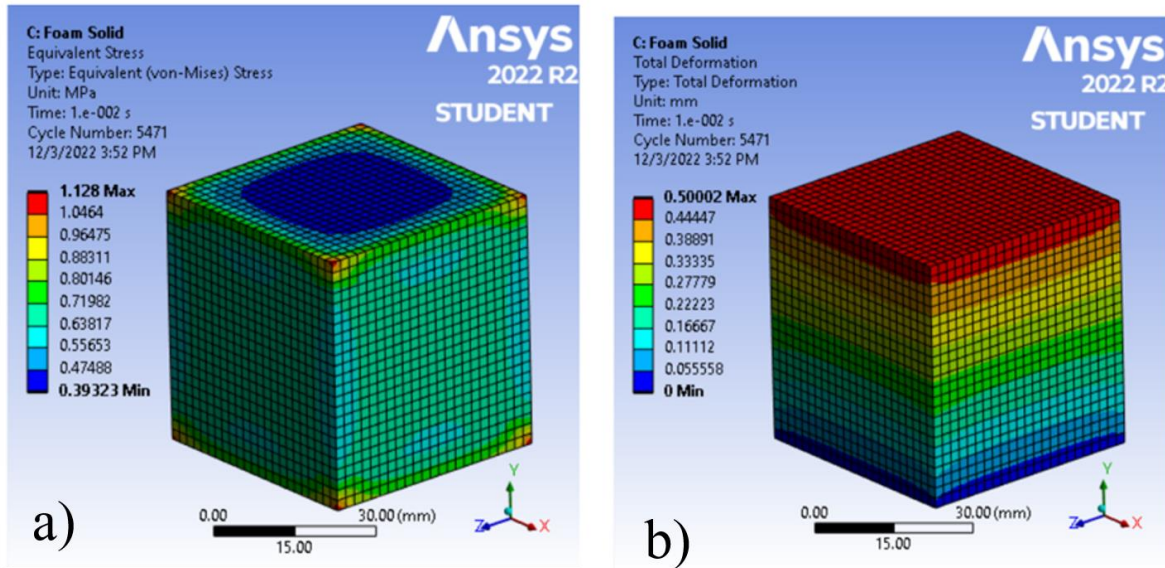


Figure 14. Plot of a) Equivalent (von-Mises) Stress Distribution and b) Total Deformation in Honeycomb for a Deformation of 0.5mm (in the -Y Direction)

The stiffness elastic model verification for all three components shows that the theoretical stiffness and FEA stiffness are similar with their percentage error all less than 10% and a maximum percentage error of 6.469% occurring in the foam model. The slight differences can be attributed to the assumptions made for the theoretical solutions. The first assumption in the theoretical calculations is that the effect of Poisson Ratio is negligible, i.e. there is no change in transverse deformation with the occurring longitudinal deformation. The second assumption made in the theoretical calculations is that the material under deformation is infinitely long. The FEA solutions do not make these assumptions. From this information, our experiment has been shown to work in the elastic region of the model with the results similar to the analytical calculations.

4.1.5 Other Plasticity Models

While the elastic-perfectly plastic model will be used primarily, strain rate dependent models, such as the Perzyna model, may be used in the case where the elastic-perfectly plastic models are not sufficient to verify the model against the existing literature, specifically with the work of R. D. Hussein et al. [9] on which our baseline models are based upon. Similarly, the foam may be modelled as a hyperplastic material if necessary.

4.1.6 Model Validation

The baseline models are validated by comparing the force-displacement curves with the experimental findings from R. D. Hussein et al [9]. This will give confidence in the simulation results of the optimized designs, where existing experimental data from literature is not available. The validation results are presented in Section 4B.

4.1.7 Optimization Plan

With a verified baseline model, optimization can begin. The model will be optimized with the goal of improving specific energy absorption. This can be accomplished in two ways: decreasing the weight of the longitudinal beam or increasing the energy absorption of its components.

The dimensioning of the honeycomb cells may be parametrically tested in order to find the dimensions which will yield the highest energy absorption. The effect of the dimension changes on the weight of the honeycomb will also be considered. Larger honeycomb cells will decrease weight while smaller honeycomb cells will increase weight.

Functionally graded (FG) honeycomb patterns show promising results in recent literature [11]. These honeycomb patterns have varying wall thickness, where wall thickness increases towards the corners of the honeycomb. Parametric testing on the ideal variation of the wall thickness will be done by implementing different iterations of FG honeycomb patterns into ANSYS and determining the change in energy absorption.

Literature has also shown promise in the use of different tube shapes [12]. While most longitudinal beams are circular, literature has shown that enneagonal tubes have higher specific energy absorption [12]. Enneagonal tubes will be implemented to the geometry and the difference in energy absorption will be determined. Furthermore, tubular vs bitubular (double tubed) beams have been explored and it was found that bitubular beams have higher energy absorption [12]. Parametric testing on the ideal number of tube layers and the ideal tube shape will be explored in ANSYS if time allows.

To reduce weight, different materials or grades of aluminum may be explored and implemented to the geometry. Furthermore, if there is sufficient time, topology optimization simulations will be done to reduce weight.

The modified designs will be compared to the baseline model for verification of optimization. This will be done both via simulation on ANSYS and by compressing 3D printed models. Using MATLAB scripts, the total absorbed energy will be derived from the area under the generated force displacement curves. Using the energy absorption values, specific energy absorption (SEA) will be calculated and used to compare the performance across modified designs.

4.2 Baseline Simulation Results and Discussion

4.2.1 Tube

A hollow tube was modeled on SOLIDWORKS and imported into ANSYS. The material model used was elastic-perfectly plastic for the tube and the material properties can be found in Table 14. A fixed boundary condition was applied to the bottom face of the square tube and a displacement boundary condition was applied on the top faces of the square tube. The displacement loading was linear from 0 to 100 mm in the direction of uniaxial compression of the geometry. A force-displacement graph was also extracted from the FEA simulations and plotted against the experimental force-displacement graph from R. D. Hussein et al [9] as observed in Figure 15. The total deformation and the von-mises stress were found and the contours were found and plotted in Figure 16 and Figure 17.

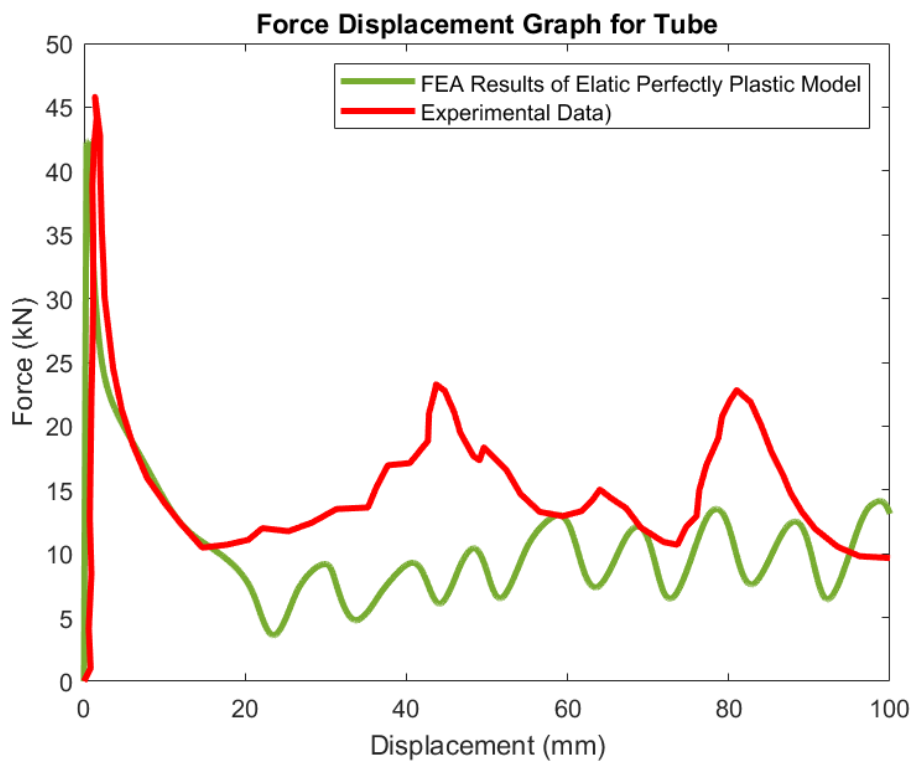


Figure 15. Force-Displacement Curve of Hollow Tube Geometry from Simulation and Experimental Data

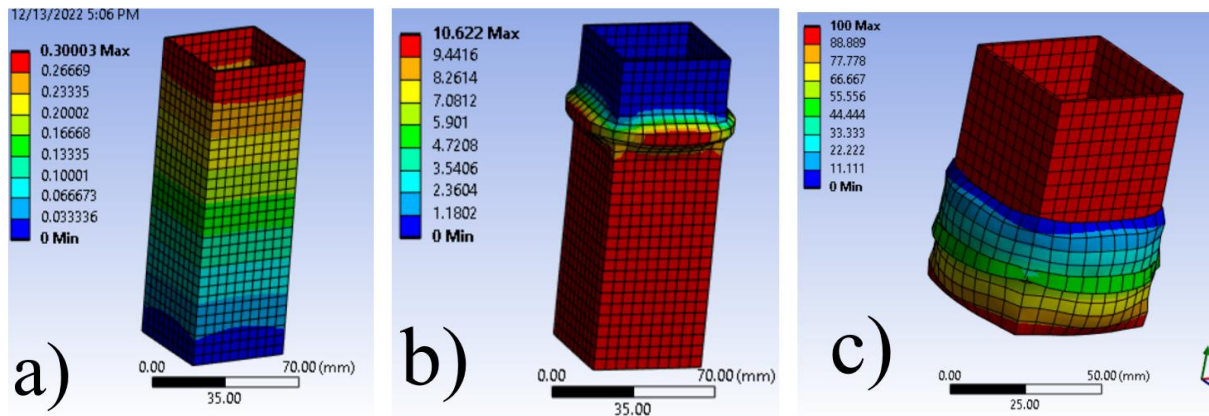


Figure 16. Hollow Tube Compression, Total Deformation Contours. (a) Before Yielding (b) Immediately After Yielding (c) After 100 mm Displacement.

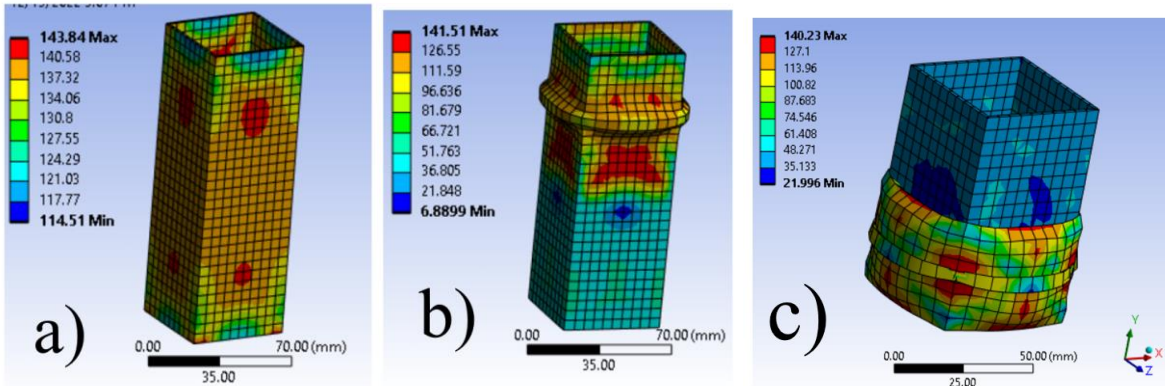


Figure 17. Hollow Tube Compression, Von-Mises Stress Contours. (a) Before Yielding (b) Immediately After Yielding (c) After 100 mm Displacement.

As can be seen, the FEA results (green line) for the hollow tube geometry varies slightly from the experimental data. Specifically, the peak force of the experimental data is 45.8 kN, while the peak force for the FEA simulation is 42.9 kN, with a percentage error of 6.33%. This percentage error validates our results as the peak forces between both plots are significantly similar with a percentage error less than 10%. However, after the deformation of the peak force, the FEA simulation also oscillates at a different force range than the experimental data. This is expected as the material model used for the geometry is elastic-perfectly plastic. Elastic-perfectly plastic assumes that the ultimate tensile strength of the material lies at its yield strength. In reality, metals' yield strength and ultimate tensile strength vary, with ultimate tensile strength occurring at a greater stress than yield strength. Thus, the elastic-perfectly plastic model is a conservative material model that underestimates the peak force and the amount of energy absorbed. The behavior after the peak force is to be explored further.

4.2.2 Foam-Filled Tube

A foam-filled tube was modeled on SOLIDWORKS and imported into ANSYS. The material model used was elastic-perfectly plastic for both the foam and the tube and the material properties can be found in Table 14. A fixed boundary condition was applied to the bottom face of both the foam and the square tube and a displacement boundary condition was applied on the top faces of the foam and the square tube. The displacement loading was linear from 0 to 100 mm in the direction of uniaxial compression of the geometry. A force-displacement graph was also extracted from the FEA simulations and plotted against the experimental force-displacement graph from R. D. Hussein et al [9] as observed in Figure 18. The total deformation and the von-mises stress were found and the contours were found and plotted in Figure 19 and Figure 20.

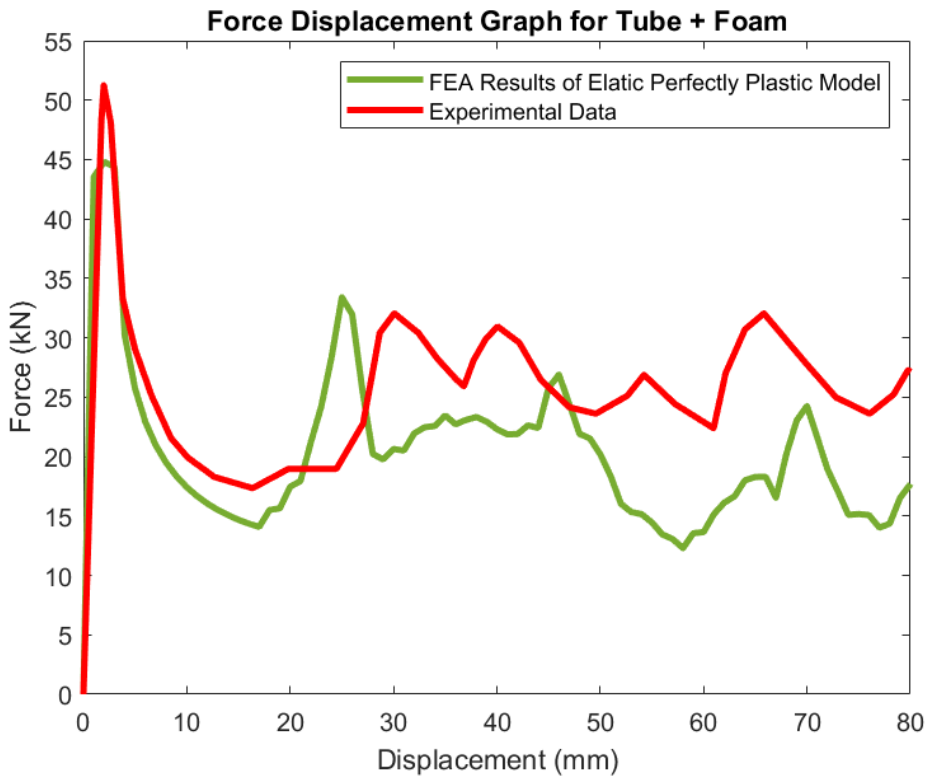


Figure 18. Force-Displacement Curve of Foam-Filled Tube Geometry from Simulation and Experimental Data

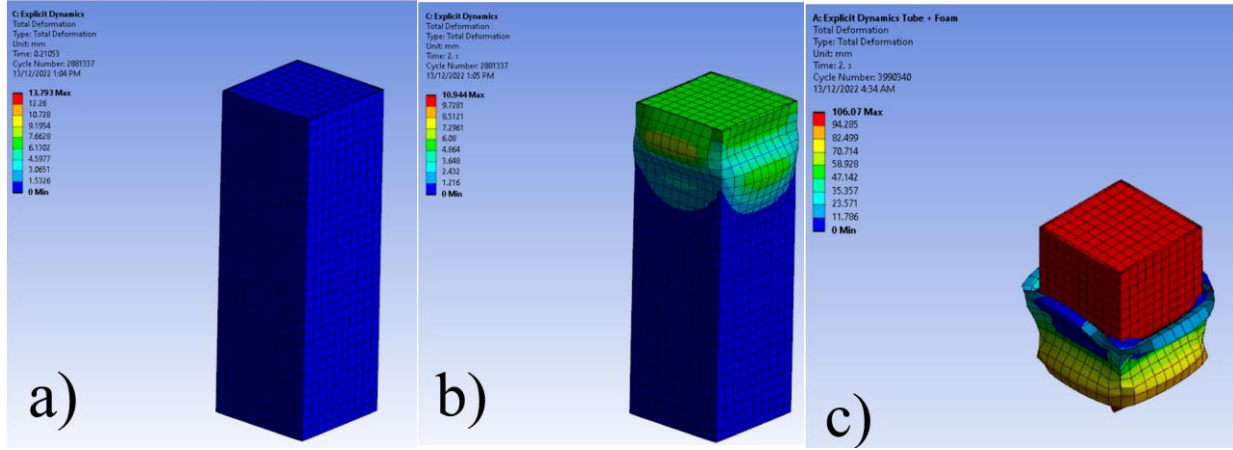


Figure 19. Foam-Filled Tube Compression, Total Deformation. Contours. (a) Before Yielding (b) Immediately After Yielding (c) After 100 mm Displacement.

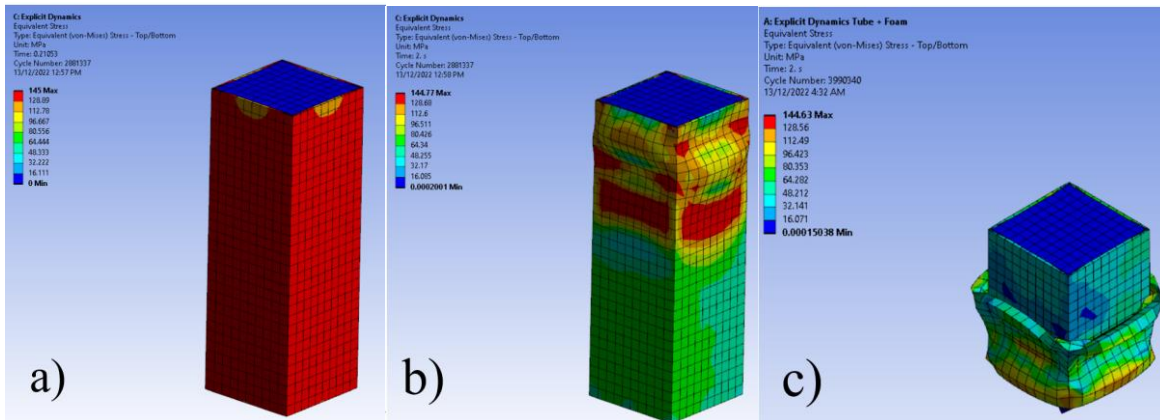


Figure 20. Foam-Filled Tube Compression, Von-Mises Stress Contours. (a) Before Yielding (b) Immediately After Yielding (c) After 100 mm Displacement.

As can be seen, the FEA results (green line) for the foam-filled tube geometry varies slightly from the experimental data. Specifically, the peak force of the experimental data is around 51.263 kN, while the peak force for the FEA simulation is around 44.803 kN with a percentage error of 12.6 %. This percentage error validates our results as the peak forces between both plots are somewhat similar. However, these variations can be expected as the material model used for

the geometry is elastic-perfectly plastic. Elastic-perfectly plastic assumes that the ultimate tensile strength of the material lies at its yield strength. In reality, metals' yield strength and ultimate tensile strength vary, with ultimate tensile strength occurring at a greater stress than yield strength. Thus, the elastic-perfectly plastic model is a conservative material model that underestimates the peak force and the amount of energy absorbed. As for the behavior after the peak force, the FEA simulation also oscillates at a different force range than the experimental data. This can be explored further.

4.2.3 Honeycomb-Filled Tube

A honeycomb-filled tube was modeled on SOLIDWORKS and imported into ANSYS. The material model used was elastic-perfectly plastic for both the honeycomb and the tube and the material properties can be found in Table 14. A fixed boundary condition was applied to the bottom face of both the honeycomb and the square tube and a displacement boundary condition was applied on the top faces of the foam and the square tube. However, due to the number of mesh elements throughout the length of the tube and honeycomb, this simulation was computationally expensive. Thus, this simulation was run up to a displacement of 3 mm (a strain of 2%) in 100 steps to capture the information on the peak force.

In Figure 21, the resulting force-displacement and peak force data value from the FEA analysis were shown and compared to the experimental peak force (value of dotted line) from R. D. Hussein et al [9]. The entire experimental graph from R. D. Hussein et al [9] was not plotted due to digitization issues arising from the thick lines used in the experimental plot. This complication is further discussed in Section-7Bb. The contours of the total deformation and the von-mises stress were also plotted in Figure 22 and Figure 23.

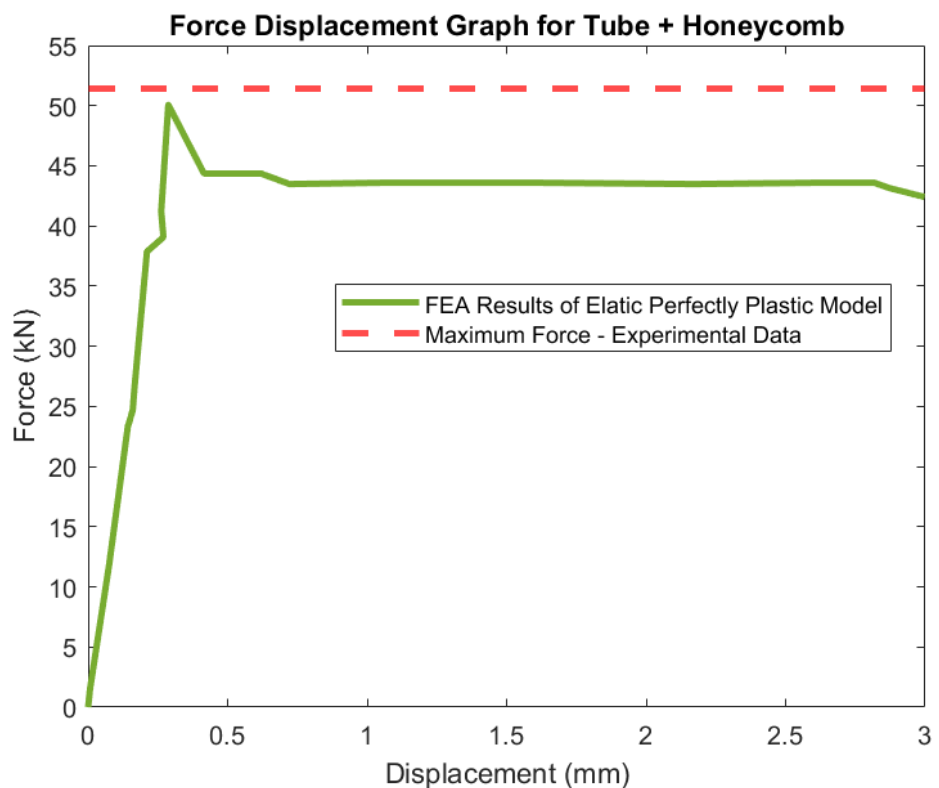


Figure 21. Force-Displacement Curve of Honeycomb-Filled Tube Geometry from Simulation and Experimental Data

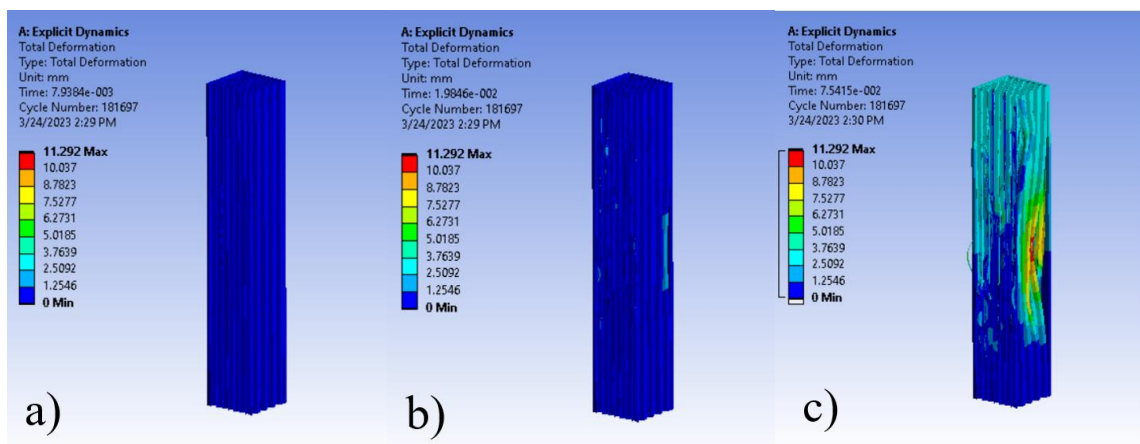


Figure 22. Honeycomb-Filled Tube Compression, Total Deformation Contours. (a) Before Yielding (b) Immediately After Yielding (c) After 3 mm Displacement.

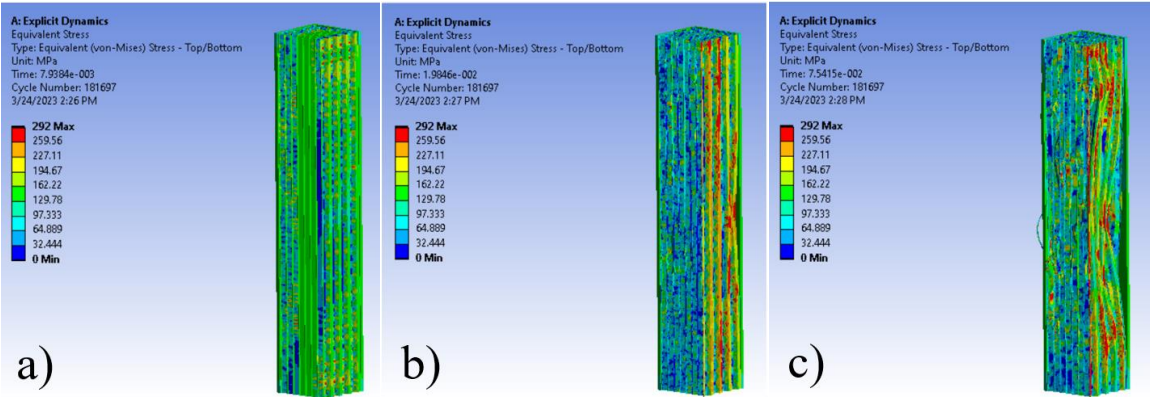


Figure 23. Honeycomb-Filled Tube Compression, Von-Mises Stress Contours. (a) Before Yielding (b) Immediately After Yielding (c) After 3 mm Displacement.

As can be seen, the FEA results (green line) for the honeycomb-filled tube geometry is similar to the experimental data. Specifically, the peak force of the experimental data is around 51.436 kN, while the peak force for the FEA simulation is around 50.712 kN. This yields a percentage error of 0.7%. Thus, the similarity between FEA and experimental peak force values suggests a high level of accuracy in the project's FEA simulations. As expected, the model undershoots the experimental peak due to the conservative nature of the elastic perfectly plastic model, which limits the material strength to its yield strength. Hardening between the yield point and maximum stress point is not considered using the elastic perfectly plastic model (refer to Figure 7), but it occurs in reality during experimentation.

4.2.4 Foam and Honeycomb Filled Tube

A foam and honeycomb filled tube was modeled on SOLIDWORKS and imported into ANSYS. A fixed boundary condition was applied to the bottom faces and edges of the composite

geometry and a displacement boundary condition was applied on the top faces and edges. As a result of the different components of this geometry, the large number of mesh elements led to high computational times. Thus, techniques outlined in Section-7Cc were used to reduce computational, and this simulation was run up to a displacement of 3 mm (a strain of 2%) in 100 steps to be able to just capture the information on the peak force.

In Figure 24, the resulting force-displacement and peak force data value from the FEA analysis were shown and compared to the experimental peak force (value of dotted line) from R. D. Hussein et al [9]. Similar to the honeycomb-filled tube baseline simulation, the entire experimental graph from R. D. Hussein et al [9] was not plotted due to digitization issues arising from the thick lines used in the experimental plot. This complication is further discussed in Section-7Bb. The contours of the total deformation and the von-mises stress were also plotted in Figure 25 and Figure 26.

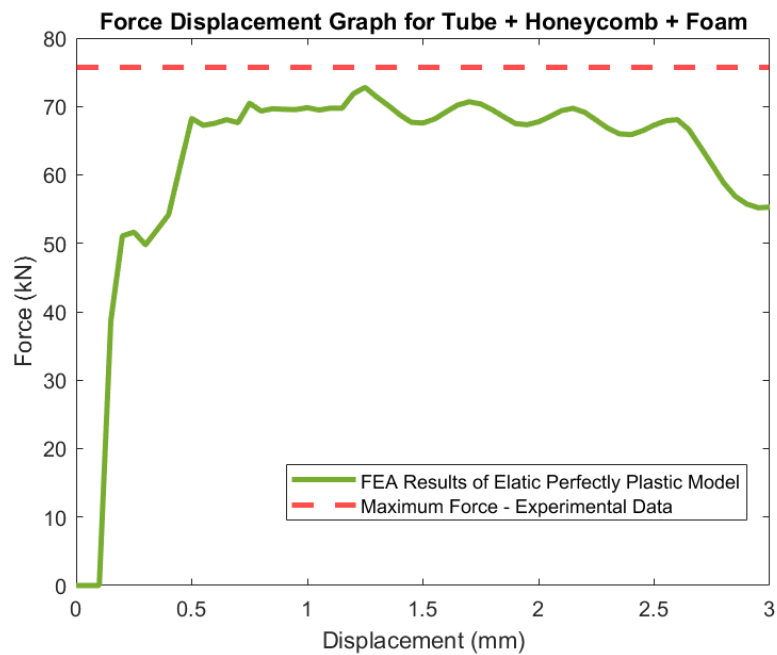


Figure 24. Force-Displacement Curve of Foam and Honeycomb Filled Tube Geometry from Simulation and Experimental Data

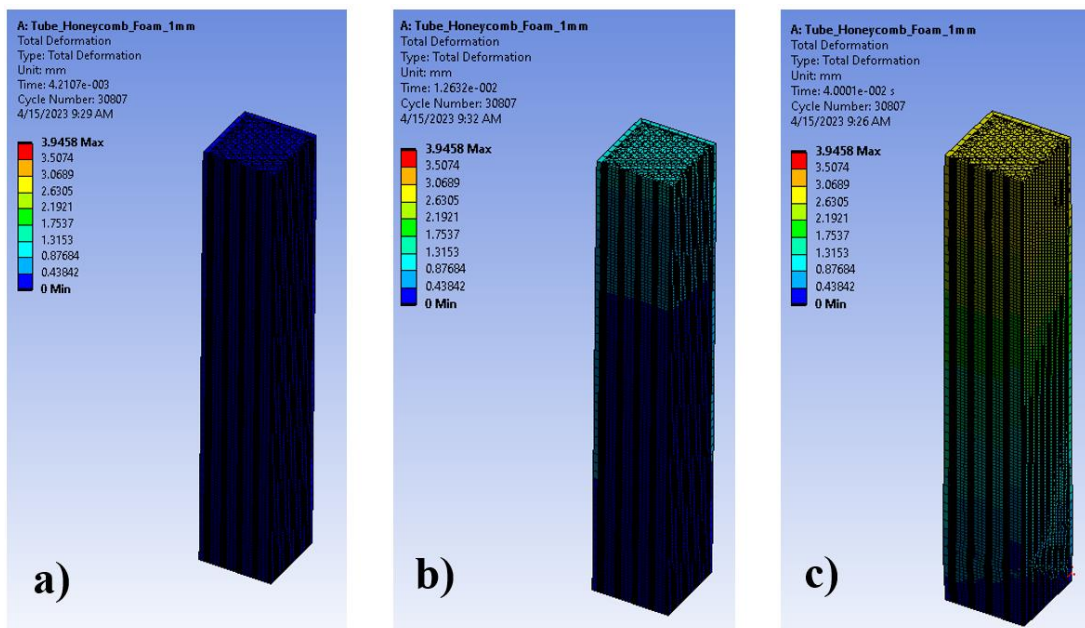


Figure 25. Foam and Honeycomb Filled Compression, Total Displacement Contours. (a) Before Yielding (b) Immediately After Yielding (c) After 3 mm Displacement.

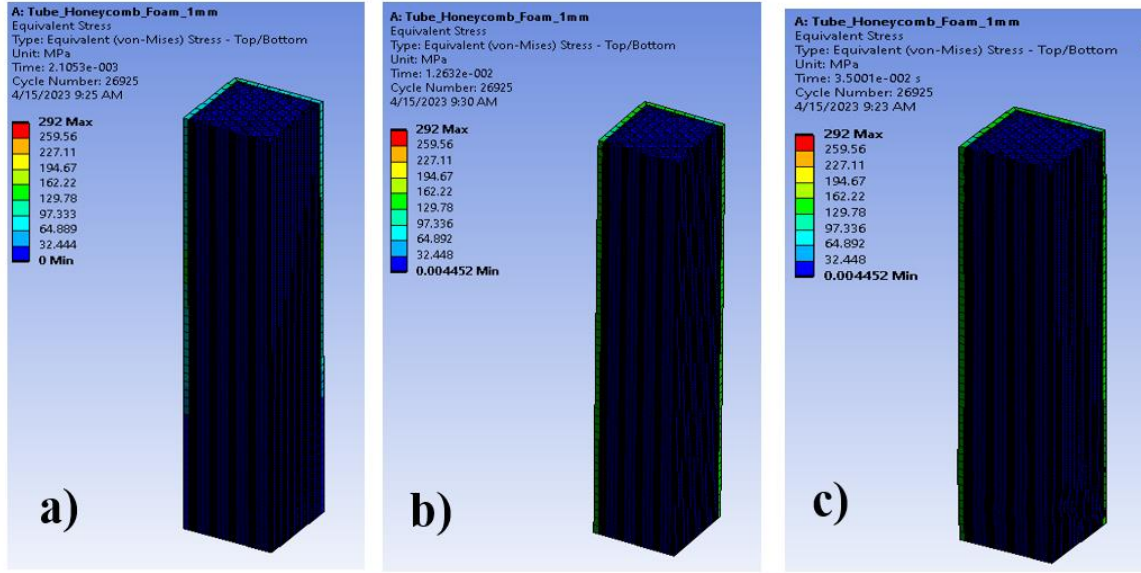


Figure 26. Foam and Honeycomb Filled Compression, Von-Mises Stress Contours. (a) Before Yielding (b) Immediately After Yielding (c) After 3 mm Displacement.

As can be seen, the FEA results (green line) for the honeycomb and foam filled tube geometry is similar to the experimental data. The peak force of the experimental data is around 75.715 kN, while the peak force for the FEA simulation is around 72.793 kN. This yields a percentage error of 3.86%. Thus, the similarity between FEA and experimental peak force values suggests a high level of accuracy in the project's FEA simulations. As explained in detail in Section 4-Bc, the conservative elastic perfectly plastic model used in simulations explains the undershoot between FEA simulation and experimental data.

4.2.5 Baseline Simulations Discussion

The baseline results served two purposes. Firstly, the results were used to confirm an acceptable level of accuracy in the simulations our project utilized to replicate the experiment from R. D. Hussein et al [9]. Secondly, the baseline results allowed the project to initially weigh

the performance of each composite (foam-filled, honeycomb-filled or both) against the composite's additional weight.

Table 15: Peak Force Comparison from FEA Simulation and Experimental Data for All Baseline Simulations

Baseline Models	Peak Force		Percentage Error of FEA Simulations (%)
	Experimental Results (KN)	FEA Results (KN)	
Tube	45.8	42.9	6.33
Foam-Filled Tube	51.3	44.8	12.6
Honeycomb-Filled Tube	51.4	50.7	0.7
Foam and Honeycomb-Filled Tube	75.7	72.8	3.86

Table 15 above shows the comparison between the FEA and experimental results for the baseline models using the peak force derived from each method to gauge the accuracy of the FEA simulations run using ANSYS. From Table 16 below, it can be observed that most of the results from the FEA simulations meet an acceptable level of accuracy of less than 10%. In the FEA simulation of the foam-filled tube, there was a percentage error of 12.6 %. This could be attributed to a number of factors. Firstly, the simulation was run up to 100 mm displacement with 100 steps. For other composites, only the first 3 mm displacement was simulated with 100 steps to save time. However, this also increased the accuracy of the peak force as there were more data points in the region of yielding. Other reasons for this significant percentage error were listed earlier in Section-4Bb. In summary, the FEA simulations using the elastic perfectly plastic model adequately represented the early yielding region of the physical compression experiment.

Table 16: Percentage Increase in Mass Observed in Composite Geometries Compared to Percentage Increase in FEA Peak Force for All Baseline Simulations

Baseline Models	Mass (kg)	Percentage Increase in Mass (%)	FEA Peak Force (kN)	Percentage Increase in FEA Peak Force (%)
Tube	0.118		42.9	
Foam-Filled Tube	0.177	50.0	44.8	4.0
Honeycomb-Filled Tube	0.155	31.5	50.7	18.2
Foam and Honeycomb-Filled Tube	0.213	80.5	72.8	69.7

Table 16 above shows the percentage increase in mass and FEA peak force observed in each baseline composite compared to the single tube model. As our baseline models were limited to accurately evaluating the peak force, we shall use the percentage increase in FEA peak force to represent the percentage increase in energy absorption expected. In order to initially weigh the energy absorption performance of each composite (foam-filled, honeycomb-filled or both) against the composite's additional weight, the percentage increase in the FEA peak force was divided by the percentage increase in mass. As such, this calculated value represents the expected percentage increase in energy absorption per unit percentage increase in the mass of the composite model. To summarize, in this preliminary study, a higher value corresponds to a greater expected energy absorption per unit additional mass.

Table 17: Percent Increase in Peak Force per Percent Increase in Mass for Baseline Composite Models.

Baseline Models	Percentage Increase in Mass (%)	Percentage Increase in FEA Peak Force (%)	<u>% Increase in FEA Peak Force</u> <u>% Increase in Mass</u>
Foam-Filled Tube	50.0	4.0	0.08
Honeycomb-Filled Tube	31.5	18.2	0.58
Foam and Honeycomb-Filled Tube	80.5	69.7	0.87

Table 17 above shows the percent increase in peak force per percent increase in mass. The least performing model was the foam-filled tube, followed by the honeycomb filled tube. A combination of both fillings however proved to be the best performing model. Though the percentage increase in mass for the foam and honeycomb filled composites was greater than the other two composites, the percent increase in FEA peak force was even greater relative to that of the two lighter composites. Using the generated peak force as a representation of the expected energy absorbed, the foam and honeycomb filled model is expected to have the greatest increase in total energy absorption per increase in mass. This result corresponds to a greater specific energy absorption (SEA) value achieved for the foam and honeycomb filled tube compared to the other composites. As such, the proposed modified designs in this project conform to the foam and honeycomb-filled tube model due to the high energy absorption and specific energy absorption values.

4.3 Proposed Modified Designs

4.3.1 Enneagonal Tube

The enneagonal tube design is a 9-sided regular polygon shaped tube. Yin et al. have demonstrated that the enneagonal tube had the highest energy absorption among various configurations [12]. Yin et al. used the outer circumcircle diameter and wall thickness as the design parameters, so we have opted to keep them constant for the enneagonal and square-shaped designs in order to make conclusions about the effect of the shape itself [12]. The circumcircle of a square is the same as its diagonal as shown below.

$$\text{circumcircle}_{\text{outer, square}} = 50\sqrt{2} = 70.71067 \text{ mm}$$

The regular enneagon was created in SOLIDWORKS by setting the circumcircle value of the polygon to be 70.71067 mm and setting the thickness of the polygon at 1.5 mm, the same as the square tube. The figure below illustrates the design of the enneagonal tube with length 50mm.

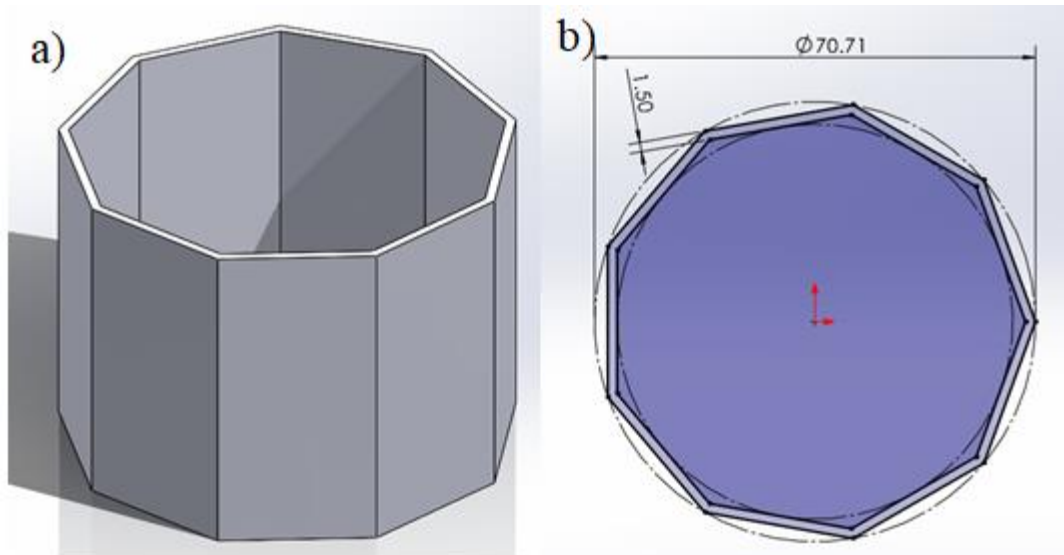


Figure 27. Enneagonal Tube Design

The above design was simulated in ANSYS. The material used is AlSi₁₀Mg of the aluminum 3D printer which will be described in more detail below. A shell mesh was created for the above design and the bottom edge was fixed. A displacement boundary condition of 35mm was applied on the top of the tube in 100 steps.

Moreover, a square tube with the same length and material AlSi₁₀Mg was simulated for comparison.

4.3.2 Constant Thickness Honeycomb Design (Control)

Due to 3D printing capabilities, the baseline constant thickness honeycomb has to be changed from the design utilized in the paper (thickness of 50.8 microns). As such, in order to compare our modified designs, a new constant thickness honeycomb was proposed with the dimensions seen in Table 18 and Figure 28 below. For square tube models, the constant thickness honeycomb occupies the same 47 mm x 47 mm x 50 mm space as the honeycomb used in the paper and the same number of honeycomb cells are present [9]. Each honeycomb cell was modeled to be regular hexagon. For the enneagonal tube model, the constant thickness honeycomb structure was modelled to have a similar bulk density to that of the square tube. This can also be observed in Table 18 below.

Table 18: Constant Honeycomb Dimension Summary.

Tube Geometry	Wall Thickness (mm)	Cross Sectional Area (mm²)	Bulk density (%)
Square	0.51	648.01	29.3
Enneagonal	0.52	977.03	29.6

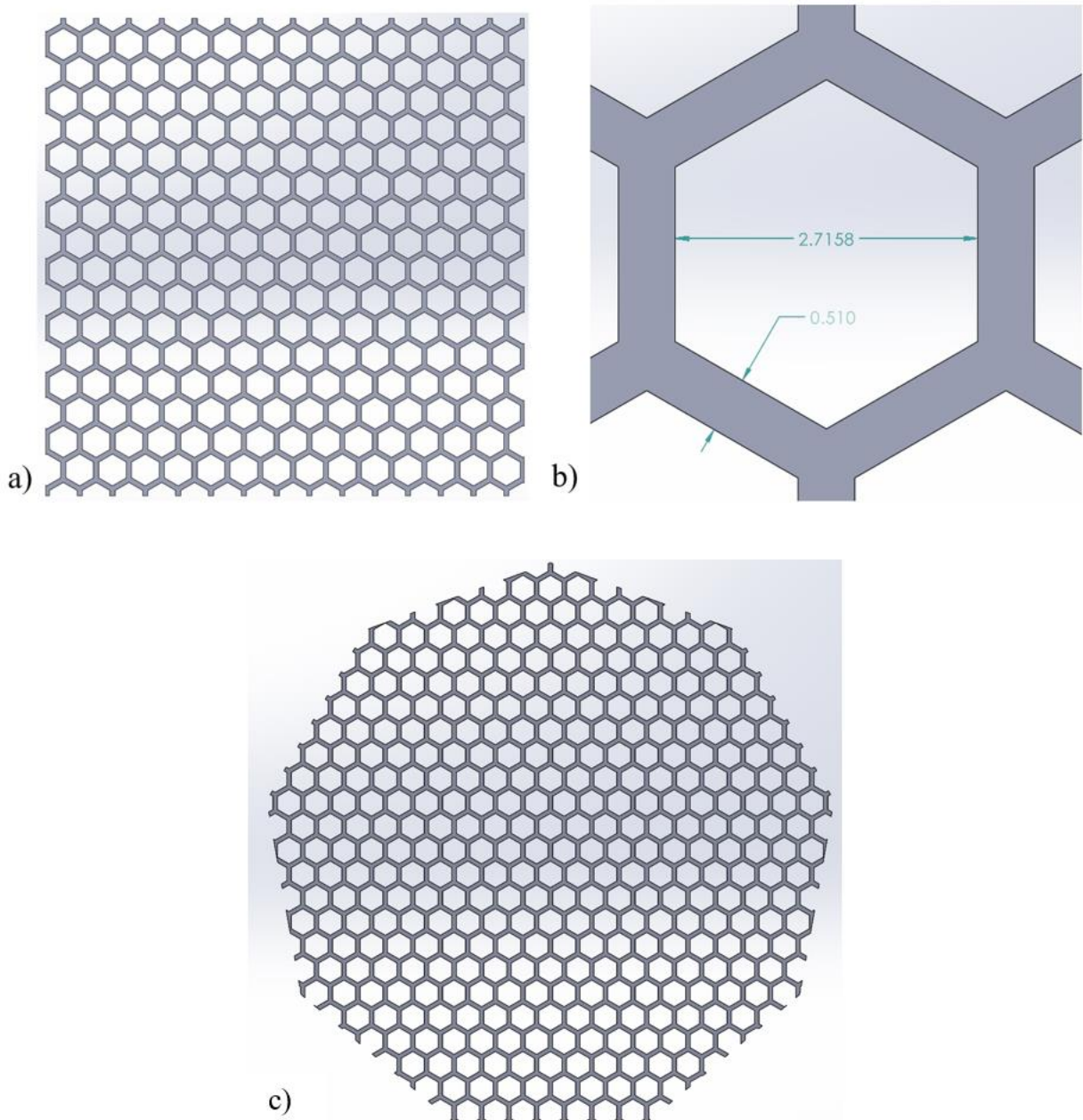


Figure 28. Dimensions for the Constant Thickness Honeycomb (in mm). (a) Total View of Cross-Section for Square Tube Model (b) Zoomed-In Image of Unit Honeycomb Cell with Dimensions for Square Tube Models (c) Total View of Cross-Section for Enneagonal Tube Model

4.3.3 Layered Honeycomb Designs

In this design, the thickness of the honeycomb cells is varied across the honeycomb geometry, increasing outwards in a concentric manner from the body's center. As such, this geometry is associated with layers, in which honeycomb cells in the same layer have the same cell thickness. The modified layered honeycomb geometries investigated in this paper consist of a 3 layered and 5 layered version. All layered honeycombs occupy the same 47 mm x 47 mm x 50 mm space as the constant thickness honeycomb geometry. Moreover, all layered honeycomb geometries were designed to have similar total cross-sectional area, volume and bulk density as the constant thickness honeycomb for uniformity. The visualization of the 3 layered and 5 layered honeycomb geometries can be seen below in Figure 29 and Figure 30 respectively. When each layer is referenced, it is made physically thicker than the others for visualization.

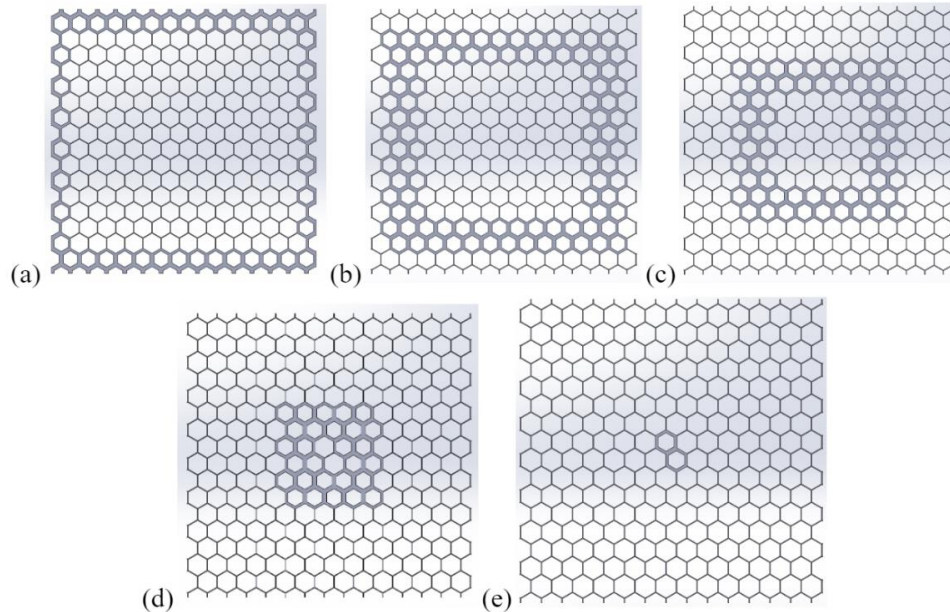


Figure 29. Visualization of the 5 Layered Honeycomb Structure - (a) Outermost Layer to (e) Innermost Layer

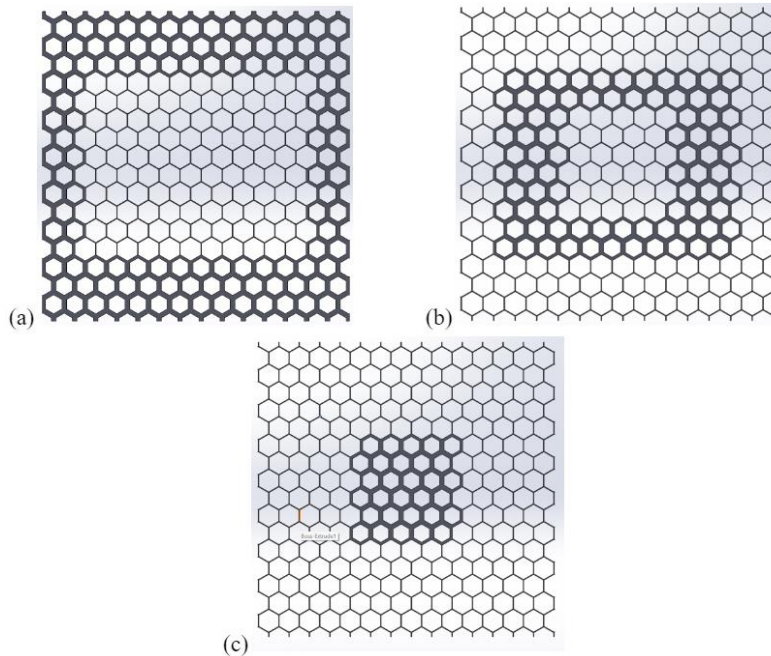


Figure 30. Visualization of the 3 Layered Honeycomb Structure - (a) Outermost Layer to (c) Innermost Layer.

For the square tube, the specific dimensions for our proposed 3 and 5 layered honeycomb designs can be seen below in Table 19a. The cross-sectional snapshot of the 3 and 5 layered honeycomb designs with the greatest differences between layers can also be seen below in Figure 31 and 32 for the square and enneagonal models respectively. For the enneagonal tube model, the layered thickness honeycombs were modelled to have a similar bulk density to that of the square tube, while maintaining the difference in the cell wall thickness across adjacent layers. In general, this led to an increase in the cell wall thickness used in the enneagonal tube models as shown in Table 19b below.

Table 19a: Square Tube Layered Honeycomb Dimension Summary.

	<i>Layer Cell Thickness (mm)</i>	<i>Diff in adj. layers' thickness (mm)</i>	<i>Cross Sectional Area (mm²)</i>	<i>Bulk density (%)</i>
<i>3 layers</i>	0.3 - 0.45 - 0.6	0.15	650.80	29.4
	0.37 - 0.47 - 0.57	0.1	650.39	29.4
	0.44 - 0.49 - 0.54	0.05	649.47	29.4
<i>5 layers</i>	0.3 - 0.375 - 0.45 - 0.525 - 0.6	0.075	643.51	29.1
	0.37 - 0.42 - 0.47 - 0.52 - 0.57	0.05	645.27	29.2
	0.425 - 0.455 - 0.485 - 0.515 - 0.545	0.03	645.34	29.2

Table 19b: Enneagonal Tube Layered Honeycomb Dimension Summary.

	<i>Layer Cell Thickness (mm)</i>	<i>Diff in adj. layers' thickness (mm)</i>	<i>Cross Sectional Area (mm²)</i>	<i>Bulk density (%)</i>
<i>3 layers</i>	0.345 - 0.495 - 0.645	0.15	980.375	29.7%
	0.4 - 0.5 - 0.6	0.10	974.276	29.6%
	0.46 - 0.51 - 0.56	0.05	976.020	29.6%
<i>5 layers</i>	0.38 - 0.455 - 0.53 - 0.605 - 0.68	0.075	978.718	29.7%
	0.425 - 0.475 - 0.525 - 0.575 - 0.625	0.05	975.147	29.6%
	0.465 - 0.495 - 0.525 - 0.555 - 0.585	0.03	978.715	29.7%

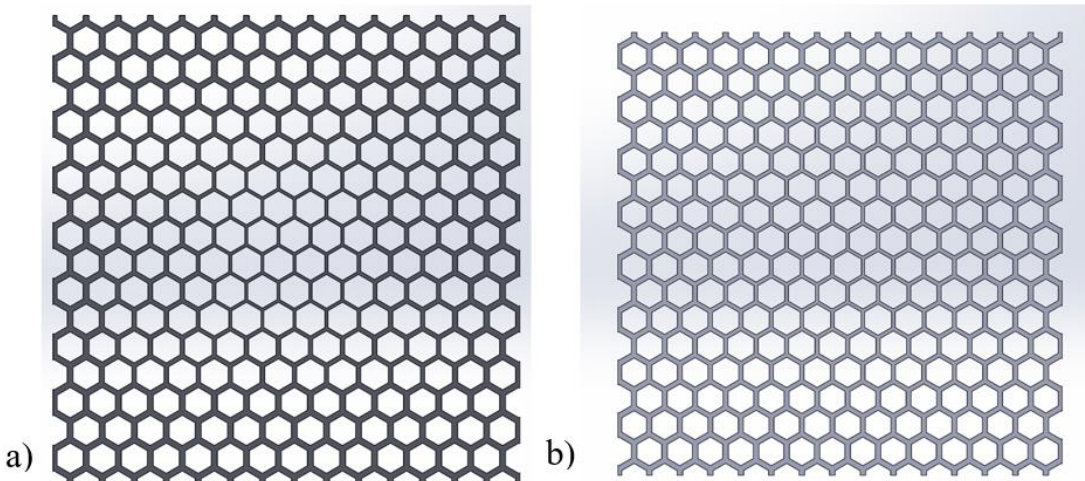


Figure 31. Layered Honeycomb Designs for Square Tube (a) 3 Layered Honeycomb Design. Thickness Increments of 0.15 mm Across Layers. (b) 5 Layered Honeycomb Design. Thickness Increments of 0.075 mm Across Layers.

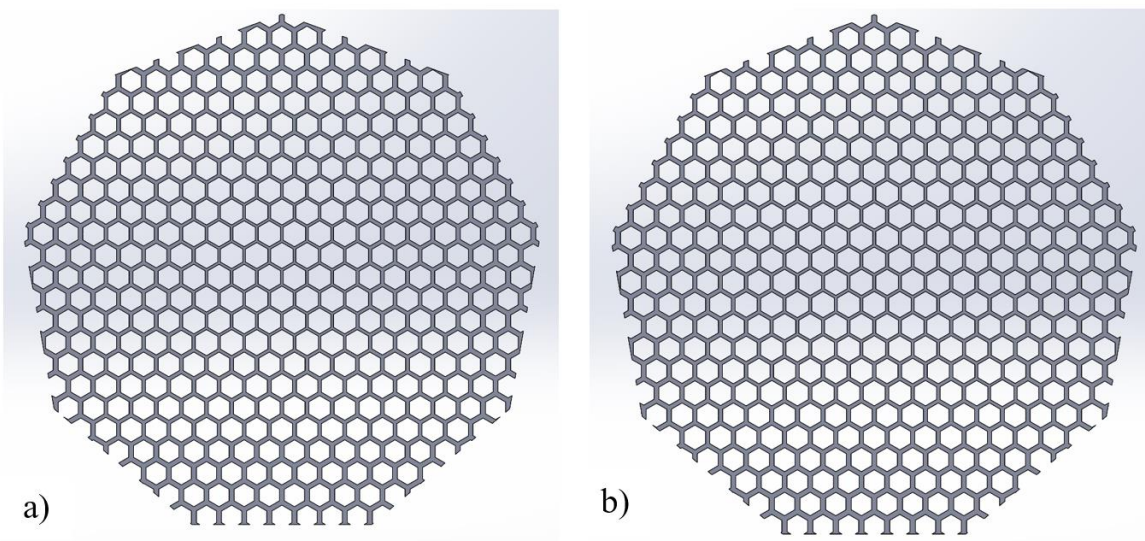


Figure 32. Layered Honeycomb Designs for Enneagonal Tube (a) 3 Layered Honeycomb Design. Thickness Increments of 0.15 mm Across Layers. (b) 5 Layered Honeycomb Design. Thickness Increments of 0.075 mm Across Layers.

4.3.4 Functionally Graded Honeycomb Designs

In this design, the honeycomb cell wall thickness was varied across the length of each individual cell wall. At the corners of each honeycomb, the thickness of the wall is at its highest, while at the midpoint of each cell wall, the thickness of is at its minimum. As mentioned before, literature has shown improved specific energy absorption in honeycombs with functionally graded thicknesses compared to honeycombs with constant thickness [11]. An example of a functionally graded thickness honeycomb is shown below in Figure 33.

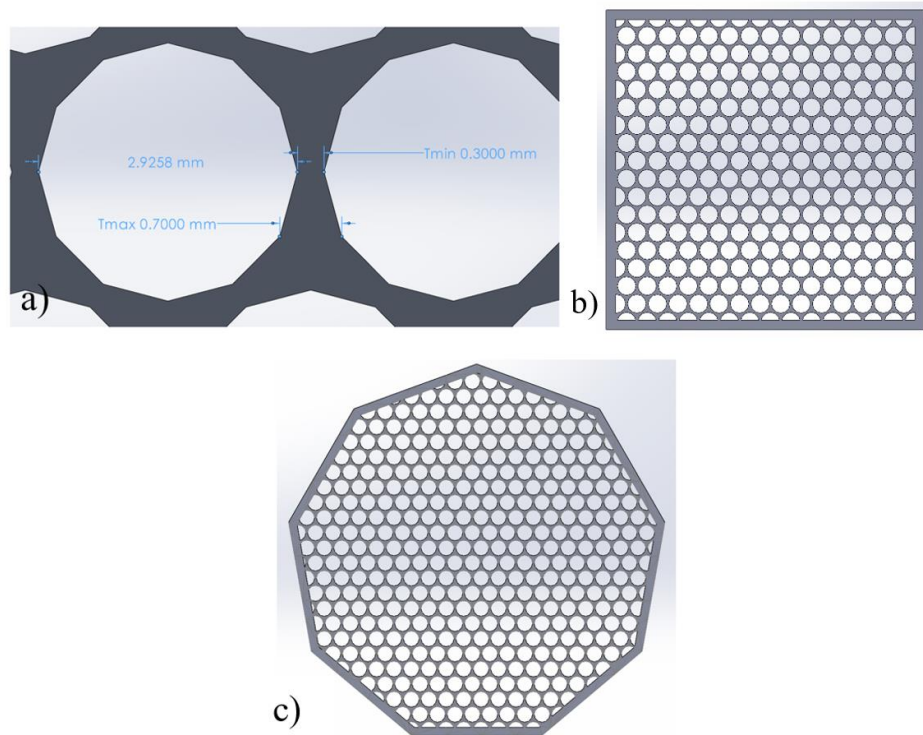


Figure 33. Functionally Graded Honeycomb Design ($T_{max} = 0.7 \text{ mm}$ and $T_{min} = 0.3 \text{ mm}$) (a) Zoomed Top View (b) Full Top View for Square Tube Model (c) Full Top View for Enneagonal Tube Model.

Three functionally graded honeycomb designs were explored in this paper, where the maximum thickness, T_{\max} , and the minimum thickness, T_{\min} , was varied. These designs summarized in Table 20 with the cross-sectional areas and relative densities of each design. For the square tube models, all functionally graded honeycomb designs occupy the same 47 mm x 47 mm x 50 mm volume as the constant thickness honeycomb for fair comparison. Furthermore, the relative densities of each design vary from 28.9% to 29.3% for uniformity. For the enneagonal tube model, the constant thickness honeycomb structure was modelled to have a similar bulk density to that of the square tube. This can also be observed in Table 20 below.

Table 20: Functionally Graded Honeycomb Dimension Summary

	T_{\max} (mm)	T_{\min} (mm)	Cross Sectional Area (mm²)	Bulk density (%)
<i>Square</i>	0.6	0.4	639.25	28.9
	0.65	0.35	642.25	29.1
	0.7	0.3	646.31	29.3
<i>Enneagonal</i>	0.6	0.4	1012.05	30.7
	0.65	0.35	995.56	30.2
	0.7	0.3	979.08	29.7

4.4 Description of Simulations for Modified Designs

4.4.1 Elastic-Perfectly Plastic Material Model

Similar to the baseline simulations, an elastic-perfectly plastic material model was used for all materials in our FEA simulations for the proposed designs. The concept on an elastic-perfectly plastic material model was described in detail in Section 5-Aa.

4.4.2 Material Properties of Components

The material properties were assigned to the components as shown in Table 19 below. A polyurethane foam of density 112 kg/m³ was used in both simulation and experimentation as this was the highest density foam that was readily available locally. AlSi₁₀Mg was assigned to both the honeycomb and tube components as this is the material that the available aluminum 3D printer utilizes. While compressive properties for AlSi₁₀Mg were available in literature [17][18][19], polyurethane foam of this specific density was not. Thus, these properties are to be found via compression testing using the Instron Universal Testing Machine.

Table 21. Material Properties For Modified Designs

	Density	Young's Modulus	Poisson Ratio	Yield Strength	Tangent Modulus
Foam (Polyurethane Foam)	112 kg/m ³	TBD	0.3	TBD	0
AlSi ₁₀ Mg	2.67 g/cm ³ [17]	76 GPa [18]	0.3897 [19]	240 MPa[18]	0

*TBD: To Be Determined

4.4.3 Setup for FEA Simulations

4.4.3.1 Geometry and Mesh Element Type

SOLIDWORKS models of proposed improved designs were created and imported into ANSYS as IGES files. Due to computational and time limitations in selecting appropriate boundary conditions, only the modified tube and modified honeycomb geometries were created and modelled as a shell bodies on ANSYS. This was done using the Midsurfacing Tool on SpaceClaim. In meshing, it was ensured that each honeycomb wall had at least 4 elements across its length to accurately capture bending and account for any potential buckling effects.

4.4.3.2 Boundary Conditions

Similar to boundary conditions in Section 4-Acii, the boundary conditions were also set to mimic the compression of a longitudinal beam during a collision. Fixed supports were added to the bottom of the geometries, while a linearly increasing displacement was applied evenly at the top edges of the geometry. The displacement conditions were then applied in a preset number of steps up to chosen maximum displacement. The maximum displacement and preset number of steps varied based on computational resources and type of experiment.

4.5 Experimental Testing of Physical Prototypes

The optimized design and the baseline design will be experimentally tested to learn more about the real behavior of the design under compressive loading. The honeycomb patterns will be 3D printed and filled with foam which will harden inside the honeycomb [9]. Then, the honeycomb

and foam combination will be put into the aluminum square tube [9]. This baseline longitudinal beam design will then be compared with the simulation values.

Next, the optimized design will be tested with the same conditions, and we can observe how much the energy absorption increases compared with the baseline experimental model as well as the simulation results.

5. Final Design Expected

The final design is expected to be a longitudinal beam with both a higher energy absorption and a lower weight as compared to the verified baseline model as described in Section 4. It is likely to contain a different honeycomb dimensioning coupled with varying wall thickness. Opting for uniform variations to wall thickness across all honeycomb cell or location-dependent variations to wall thickness will depend on the simulation and experimental results. These results will also determine the specific wall thickness measurement variations. The final design is also likely to be an enneagonal tube design with both honeycomb and foam within each tube layer if the optimization testing proves that these changes are valuable. The materials chosen for the tube/honeycomb and the foam may vary from the baseline model materials. Figures 34 and 35 are models of the individual components of the possible final design described above.

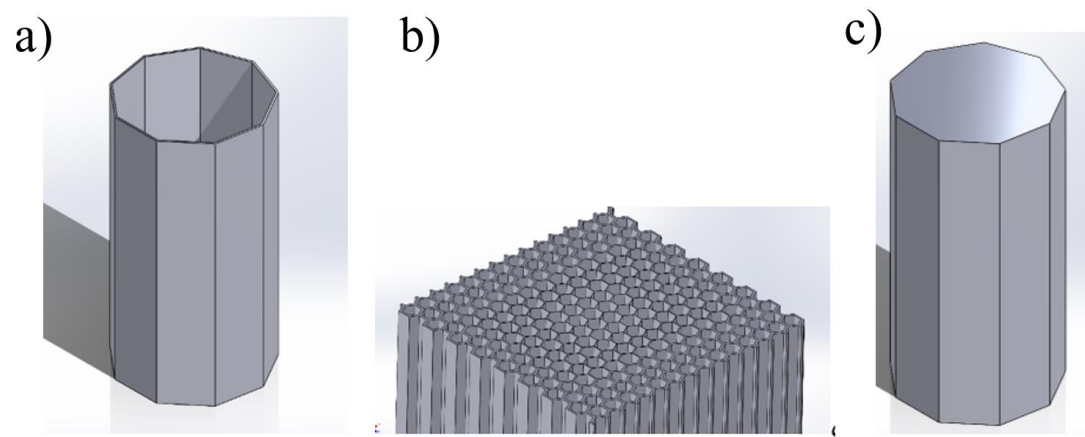


Figure 34. Expected Optimized Shape. (a) Enneagonal Tube (b) Functionally Graded Honeycomb (c) Foam

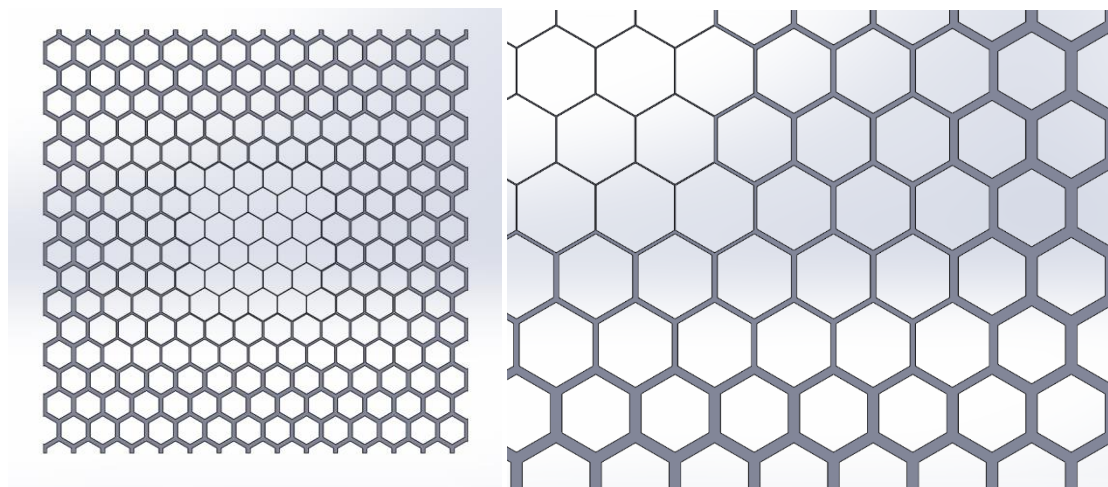


Figure 35. Top Views of Layered Honeycomb Component

6. Budget

The below materials will be used in our designs. Note that the quantity is described per each design so the real quantity will be dependent on the number of experimental tests we perform.

To garner a cost estimate, we have reached out to the materials lab which will aid us with that. In the meantime, the cost values below are estimated from web sources.

Part #	Part Name	QTY	Function	Mass (g)	Material	Manuf. Process	Dimensions	Cost per piece
1	Square Tube	1	Energy Absorption	114.9/piece	Aluminum alloy AA 6060-T5)	NA	Inner side length 47mm, avg. tube wall thickness 1.5 m. Length 150mm	\$2.62
2	Honeycomb	3	Energy Absorption	14.8/piece	Aluminum HexWeb® CR III aluminium alloy 5052 with an H39 temper	NA	Specification 8.1-1/ 8– 5052-.002N	\$1.50
3	Foam	3	Energy Absorption	17.2/piece	Rigid polyurethane foam (Polyol & Isocyanate)	Polyol and Isocyanate mixed in 1:1 ratio, poured into a square mold	[47mm sides, 50mm length]	\$.59

7. Implementation Details

7.1 Progress Summary on Proposed Design

The process of implementation has ultimately been successful thus far. Despite issues such as item procurement, computational expense, and 3D printing capabilities, necessary changes have been made to both design geometry and materials in order to proceed. For computational expense issues and the complexity of designs in simulation, various meshing and simulation techniques were used to cut computational time drastically and experimental compression will be done in place of simulation when necessary. Furthermore, through trial and error, various 3D printing issues have been resolved and optimal printing orientations and support requirements have been noted. The FEA simulation results have shown enneagonal tubes to superior to square tubes in terms of peak crush force and specific energy absorption. As for layered honeycomb and functionally graded designs, there are negligible differences in peak crush force and specific energy absorption in comparison to constant thickness honeycomb results. Deeper insight to the changes in energy absorption for the designs will be found via experimental compression of 3D printed specimen.

7.2 Issues Faced During Implementation/Experimentation

7.2.1 Computational Expense

Due to the use of non-linearity of the mechanics involved, computational time of the more complicated geometries exceeded available computational resources. The set recommended time for our preliminary simulations was between 5 to 10 hours. With some of these complex simulations reaching multiple days or weeks, necessary

measures had to be sought out to reduce the time and computational resources needed for the FEA analysis. Further explanation of the measures taken to reduce computational expense is provided in section 7.3.

7.2.2 Complexity of Initially Proposed Geometries

Shell elements were chosen for this project due to the significantly low thickness to length ratio of the cell walls. As such, solid bodies were not advisable as there is a need to create at least 4 elements across the thickness of the already thin honeycomb cell walls. Using solid bodies thus resulted in poor quality meshes (high aspect ratios) or extremely fine meshes which demanded high computational resources.

Hence, investigation on the proposed functionally graded honeycombs was halted as expressing the geometry as a shell body with a thickness proved challenging. This is because of the changing thickness across the cell wall. Other measures to successfully simulate this geometry using FEA software are currently being looked at. However, if these measures prove to be time-consuming or inaccurate, the investigation of the functionally graded honeycomb would be conducted solely through physical compression.

7.2.3 Item Procurement

Initially, to experimentally test the different geometries, both baseline and optimized, using the Instron Universal Testing Machine, the following materials were required:

1. Polyurethane foam of density 180 kg/m^3
2. HexWeb Honeycomb with specification of 8.1-1/8-5052.002. The required material is Aluminum Alloy 5052 with an H39 temper.

3. Aluminum tube manufactured from Aluminum Alloy AA 6060-T5

However, there were no available polyurethane foam systems locally with a density of 180 kg/m³. Available local polyurethane foam systems were all of lower density. Due to time constraints and the complications of international shipping, international sources were not considered. Similarly, the procurement of the honeycomb from HexWeb and the aluminum tube could not be done due to the issue of time expense and the complications of international shipping. Aluminum Alloy AA 6060-T5 tubes were not available locally. Furthermore, available aluminum 3D printers could not print these geometries with the required material. Instead, the aluminum printer uses AlSi₁₀Mg. For these reasons, it was necessary to use different materials from the literature [9].

7.2.4 Acquiring Specific Material Properties from Baseline Papers

The baseline properties were found via graph digitization. The literature contained force-displacement curves that were used to find values for Young's Modulus and Yield Strength [9]. As an example, the force-displacement curve for Aluminum Alloy 5052 with an H39 temper is shown in Figure 36. Due to the line thickness of the plot and the absence of raw data, graph digitization is naturally somewhat inaccurate. This issue particularly noticeable when comparing experimental data to FEA results for the honeycomb-filled tube.

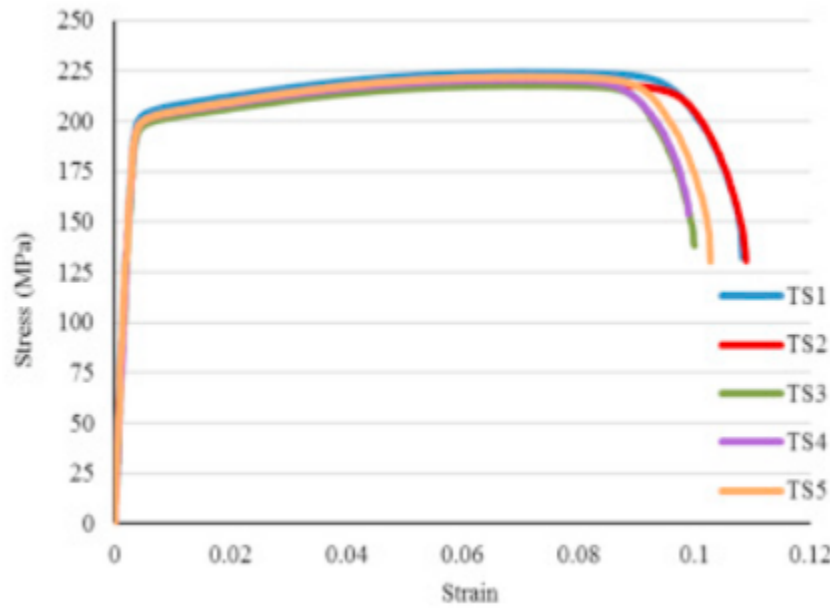


Figure 36. Literature Force-Displacement Curve for Aluminum Alloy 5052 with an H39 temper from Literature [9]

7.2.5 3D Printing Capabilities and Resolution

The original 3D printing plan of this project was to make use of the Formiga P110 and aluminum printer. The Formiga P110 would have provided relatively fast printing times and a ductile plastic material suited for our compression tests (PA2200). In addition, the aluminum printer would have provided realistic material choice though with slower printing times in comparison to Formiga P110. However, both of these printers were out of service during our project. Due to laser and/or wire EDM issues, both printers could not be used and instead the Form 2 Desktop Stereolithography 3D printer was opted for. The Stratasys F370 printer was tested as well, but there were various inaccuracies in the honeycomb pattern due to the resolution of the printer as shown in Figure 37.

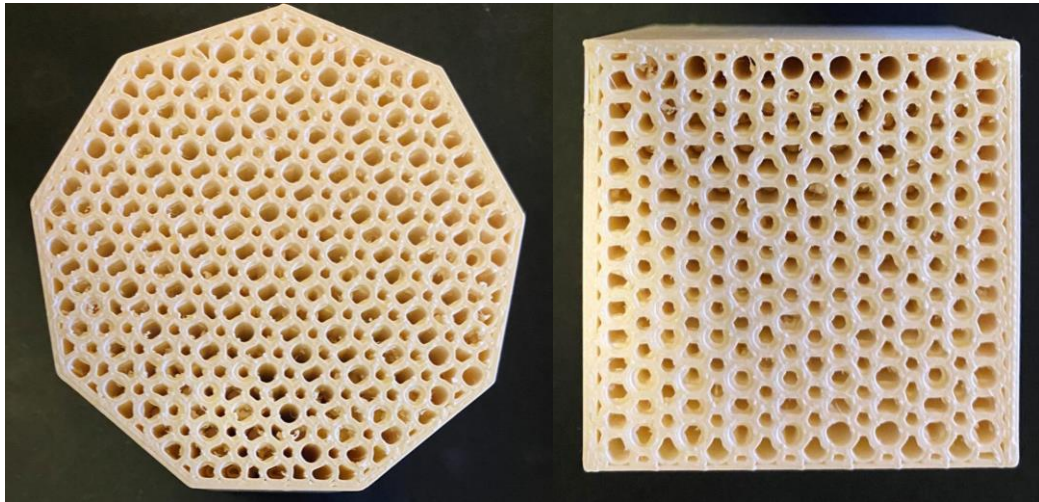


Figure 37. F370 Print Inaccuracies

As seen in the figure, the honeycomb structure is inaccurate and non-uniform. Thus, the F370 was no longer used. It is important to note that the Form 2 Desktop Stereolithography 3D printer machine provides slower printing times in comparison to the aluminum printer, limiting the volume of samples that can be ultimately tested. The allowable thickness of the Form 2 printer is 250 microns. Thus, the baseline honeycomb design from literature could not be tested as its wall thickness is 50.8 microns [9]. Thus, the honeycomb had to be changed to meet the minimum resolution.

7.2.6 Printing Errors and Chipping

Initially, the models were 3D printed in the vertical orientation, meaning that the top view of the honeycomb was printed in layers. However, upon doing this, inaccuracies in the honeycomb pattern were found as shown in Figure 38. Some cells were filled with resin while others were smaller than intended in the design.

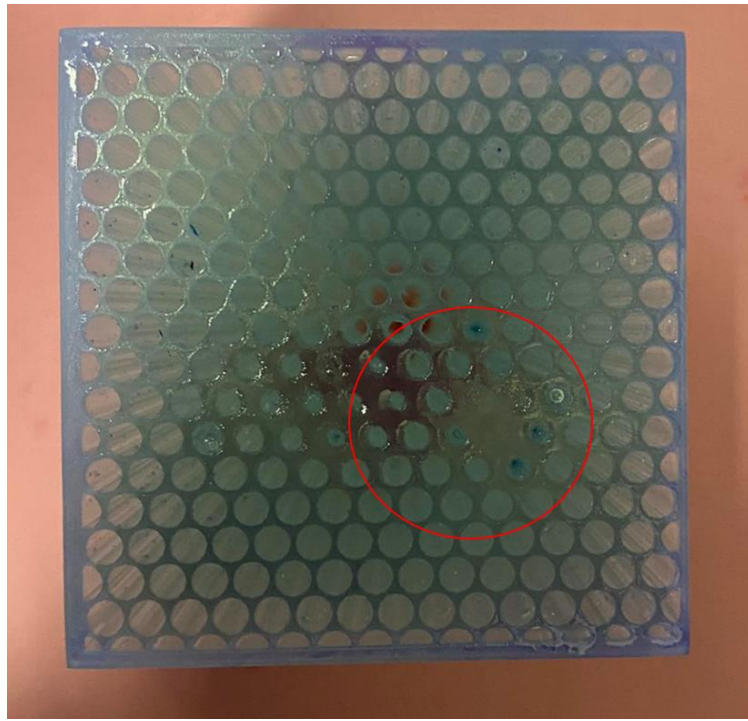


Figure 38. Form 2 Vertical Printing Orientation Inaccuracy

The design was then printed horizontally, meaning that the tube-side of the honeycomb was printed first. Upon doing this, the print had fallen off of the build plate, indicating that supports may be required. Thus, supports were implemented to the print. This solved the issue and horizontal printing yielded no inaccuracies in the honeycomb pattern. However, the print experienced damage upon the manual removal of supports as shown in Figure 39.

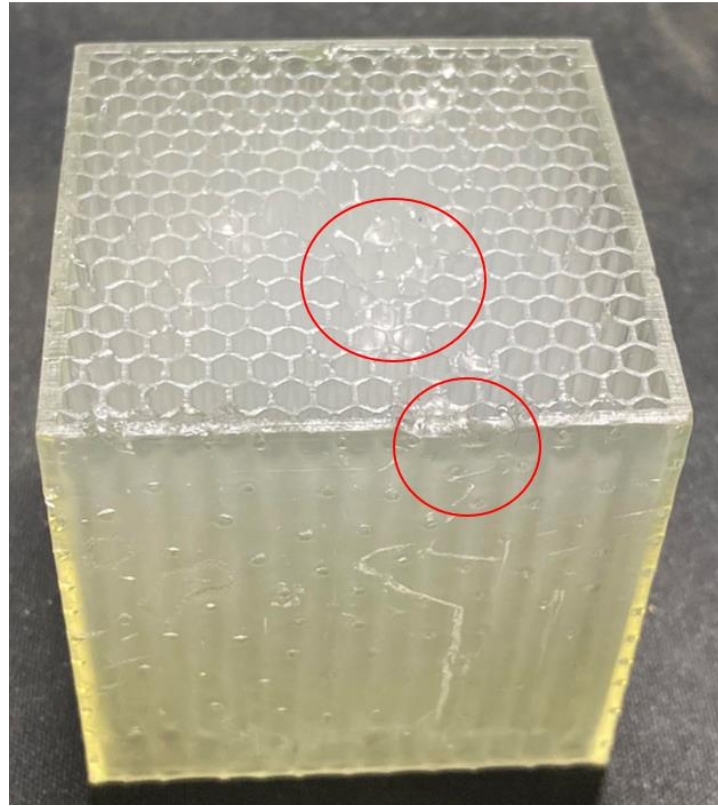


Figure 39. Damage to 3D Print Due to Manual Removal of Supports

7.3 Adjustments Made During Design Implementation

7.3.1 Changes Made During Simulation Implementation

7.3.1.1 Material and Design Changes

Due to the aforementioned challenges posed by 3D printing, the material and design of our simulations were adjusted accordingly as described in Section 5. Furthermore, a polyurethane foam of density 112 kg/m^3 will be used instead of 180 kg/m^3 due to previously mentioned issues of foam procurement. The properties of AlSi₁₀Mg and polyurethane foam were outlined in Table 21.

Moreover, an original constant wall thickness design was created and tested in order to act as a new baseline for comparison to optimized designs. This new constant

thickness design was created to account for the printing resolution issue where the minimum allowable thickness is 300 micrometers. The design of the simple constant thickness honeycomb is shown below in Figure 40 where the wall thickness is 510 micrometers.

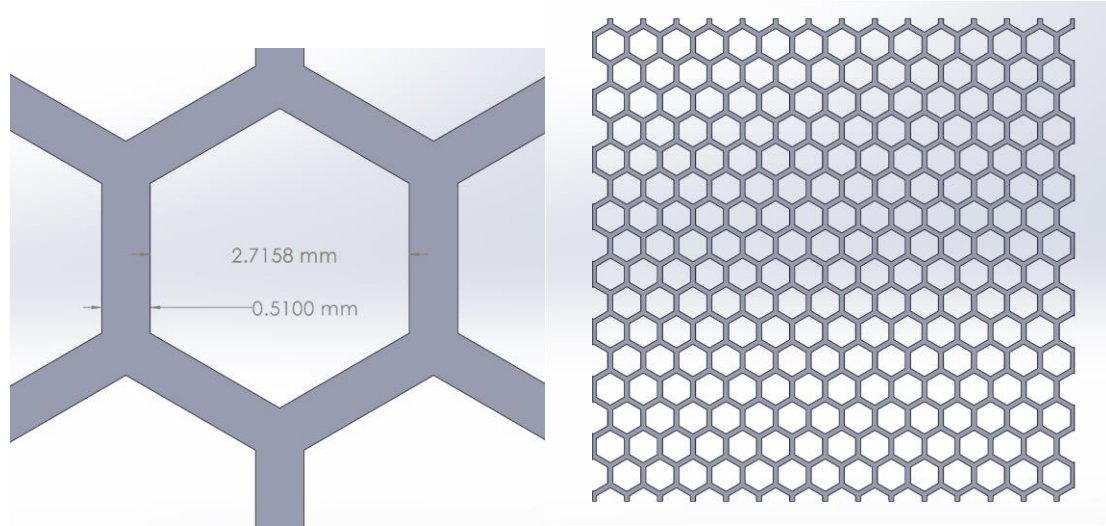


Figure 40. Constant Thickness honeycomb modified for 3D printing

7.3.1.2 Symmetry, Mass scaling, and Meshing to Reduce Computational Cost

To save computational time, three main measures were considered symmetry, mass scaling, and the investigation of minimal mesh elements required to acquire reasonable results. These concepts are explained below.

Symmetry: As all models were symmetrical, only a quadrant of each model was simulated with a roller boundary condition placed on the edges/faces where the cut was made. As such, all results obtained needed to be scaled up by a factor of four to derive the true force-displacement curves of the model. Figure 41 below shows how each model is divided in order to utilize symmetry.

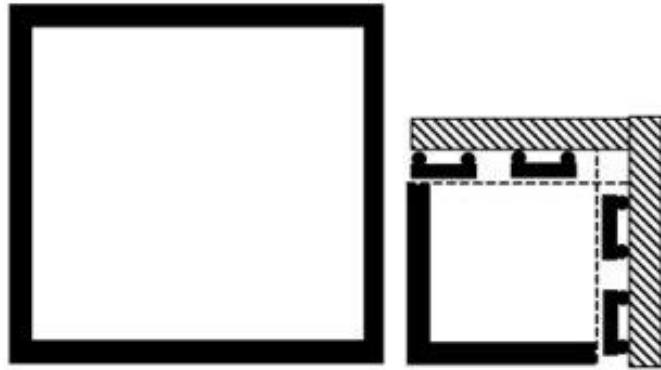


Figure 41. Diagram Showing Use of Symmetry in the Simple Tube Model

Mass Scaling: The density of materials for all materials was multiplied by a common factor to increase the computational time step. Further investigation for the mass scaling effect was carried out using the baseline tube and foam-filled tube model to determine an appropriate scale factor that could increase speed and maintain accuracy. For both the tube and foam-filled tube simulations, six simulations were repeated at a mass scaling of 1 (original density), 10, 100, 1000, 10000, 100000. Force-displacement curves were derived up to a maximum displacement of 5 mm in 100 steps to achieve more accurate data near the peak. The generated force displacement graphs for both the tube and foam-filled tube simulations can be seen in Figure 42 below. From this investigation, the chosen mass scaling for simulations with high computational demand was set to a maximum of 1000. Beyond a mass scaling of 1000, the force-displacement curve around the yielding point deviated significantly.

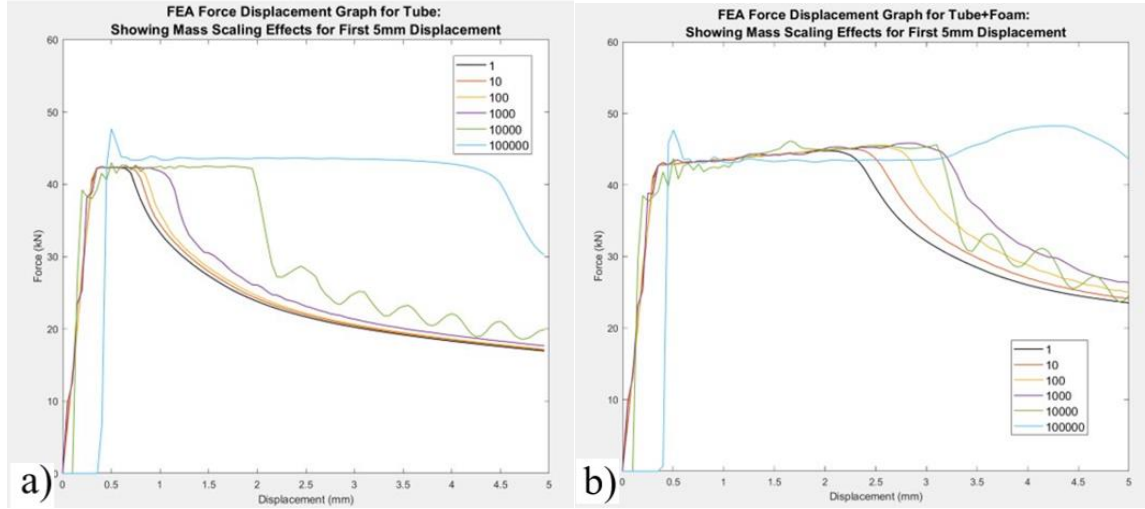


Figure 42. Force-Displacement Graphs for (a) Tube and (b) Foam-Filled Tube Simulations at Different Mass Scaling Factors.

Exploration on Mesh Dependence: The number of elements along the length of a wall affects the simulation's ability to accurately capture buckling. Local buckling was expected in the honeycomb geometry due to the significantly high length to thickness ratio. Honeycomb meshes with greater than 4 elements per cell wall were compressed in simulation and their results were compared to honeycombs with 4 elements. Results showed negligible difference in results as the elements per cell wall increased beyond 4, though simulation time increased significantly. This indicated that 4 elements were sufficient to accurately capture buckling effects. As such, for simulations with high computational load, the mesh was created to have 4 elements per cell wall in order to save time and maintain accuracy. Figure 43a below shows an example of the honeycomb mesh with 4 elements per side that was opted for while Figure 43b shows a more computationally expensive and finer honeycomb mesh with 8 elements per side.

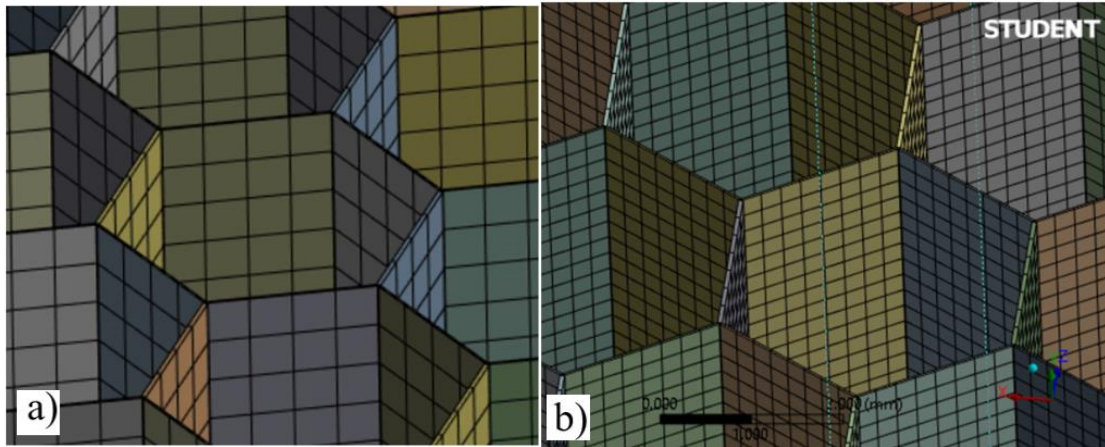


Figure 43. Meshing Showing (a) 4 elements per Hexagon Side and (b) 8 elements per Hexagon Side

Smaller Sample of Geometry for Functionally Graded Honeycomb

The functionally graded honeycomb design posed problems for modeling the geometry with shell elements. Due to the lack of a uniform cell wall thickness, using shell elements would be very complex. Thus, at least 4 solid elements through each thickness were opted for instead. However, this increased simulation drastically due to the high number of elements and required further measures than symmetry and mass scaling. Thus, instead of modeling a 50mm x 50mm x 50mm honeycomb, a 5 mm x 5 mm x 5 mm honeycomb was modeled instead. While peak crush force values and energy absorption values would not be comparable to other 50 mm x 50 mm x 50 mm simulations, valuable conclusions on the influence of functional grading could still be made. The full geometry was still opted for during experimental testing.

7.3.2 Changes Made During Experimental Implementation

7.3.2.1 Changing Printing Orientation

Initially, the part was printed vertically in a regular fashion which did not require any supports. However, upon inspecting the printed part, the honeycomb pattern in the center was not uniform and some cells were filled in with the print material. The print orientation was changed to print the part horizontally with the side of the tube facing the build plate due to the printer's superior resolution in that print plane. This change solved the aforementioned problem but required many supports to be added in order to hold the part from falling off the build plate. Initial touchpoint size and support density at this stage were about 1.3mm and 0.9 respectively.

7.3.2.2 Decreasing Touchpoint Size and Support Density

After adding more supports, the problem of removing them post-print emerged. In the first iteration of the new printing orientation, the part was slightly damaged in the support removal process. However, it was important to still add sufficient supports to avoid the part falling off the build plate. In order to decrease damage to the print during the removal of supports, the touchpoint size was decreased to 0.9mm which allowed for an easier support removal and less chipping of the part.

7.3.2.3 Printing Fewer Geometries

In order to account for the increased printing times of the Form 2 printer, not all of the simulated geometries were printed for experimental testing. Instead, the following were printed: constant thickness honeycomb-filled tube, two functionally-graded honeycomb-

filled square tubes, and two five layered honeycomb-filled square tubes, one functionally-graded honeycomb-filled enneagonal tube, and one five layered honeycomb-filled enneagonal tube. This yields a total of seven prints in contrast to the initially intended 22 prints.

7.4 Initial Results for Modified Designs

7.4.1 Enneagonal Tube Results

Using ANSYS explicit dynamics, the modified enneagonal tube was compressed up to 35mm in 100 steps. A simulation experiment was performed on the original square tube. Force-displacement curves were generated from both simulations. Using MATLAB, the FEA peak force and energy absorbed (area under curve) was calculated and compiled in Figure 44 and Table 22 below. These values were then used to draw initial conclusions between the performance of the square and enneagonal tubes. The enneagonal tube demonstrates a higher force peak as well as higher energy absorption.

Moreover, the specific energy absorption becomes relevant in this comparison due to its independency from the mass. The mass was found by calculating the volume of material in each tube and using the material density 2.67 g/cm³. The enneagonal tube demonstrates significantly higher SEA than the square tube.

$$SEA = \frac{Energy\ Absorption}{Mass}$$

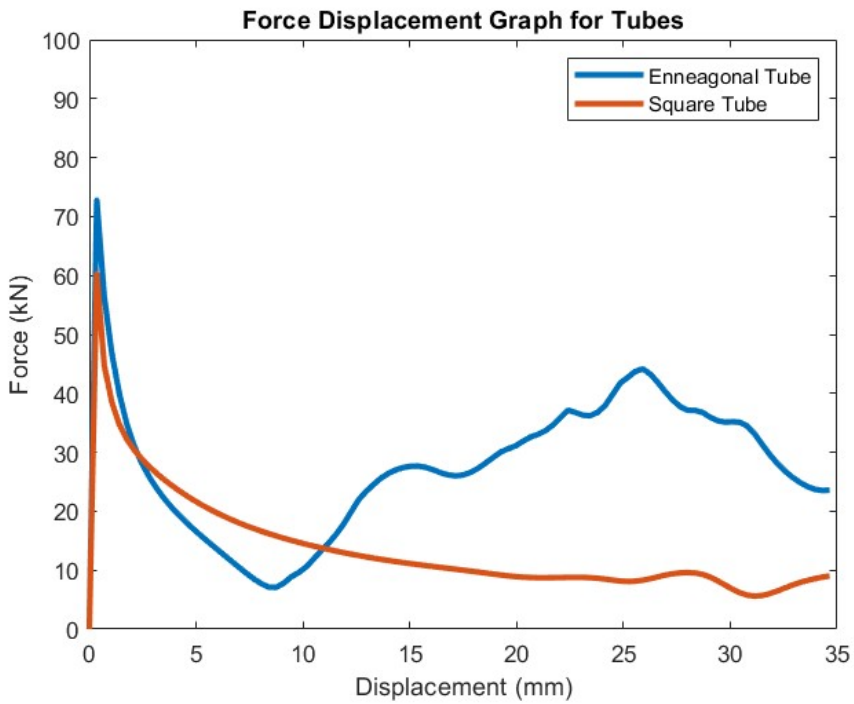


Figure 44. Force Displacement Curve for Enneagonal and Square Tubes

Table 22. FEA Results for Modified Tube Design

Simulation	Peak Force (kN)	Energy Absorbed in 35mm (J)	Mass (g)	Specific Energy Absorption (J/g)
Square Tube	60.324	473.779	38.85	12.20
Enneagonal Tube	72.793	959.681	42.603	22.53

7.4.2 Layered Honeycomb Results

ANSYS simulations were performed for the modified 3 and 5 layered honeycomb fillings. In these simulations, the geometries were compressed up to 2.5mm in 100 steps, so as to gather accurate information around the yielding region of these geometries such as the peak force. Force-displacement curves were also generated from the solutions and are seen in Figure 45 and Figure 46 below. Using MATLAB, the FEA peak force and energy absorbed (area under curve) in the first 2.5 mm was derived and compiled in Table 23 below. These values were then used to draw initial conclusions on the 3 and 5 layered designs.

The data from Figure 45, Figure 46 and Table 23 reveals that both the peak force and the energy absorbed are not significantly different between the constant thickness geometry and all layered honeycomb designs. Experimental compression testing may be needed to determine the accuracy of the findings regarding energy absorption, which are not highly dependable due to the unreliability of the material model after yielding.

FEA Force Displacement Graph for 3 Layered Honeycomb Designs

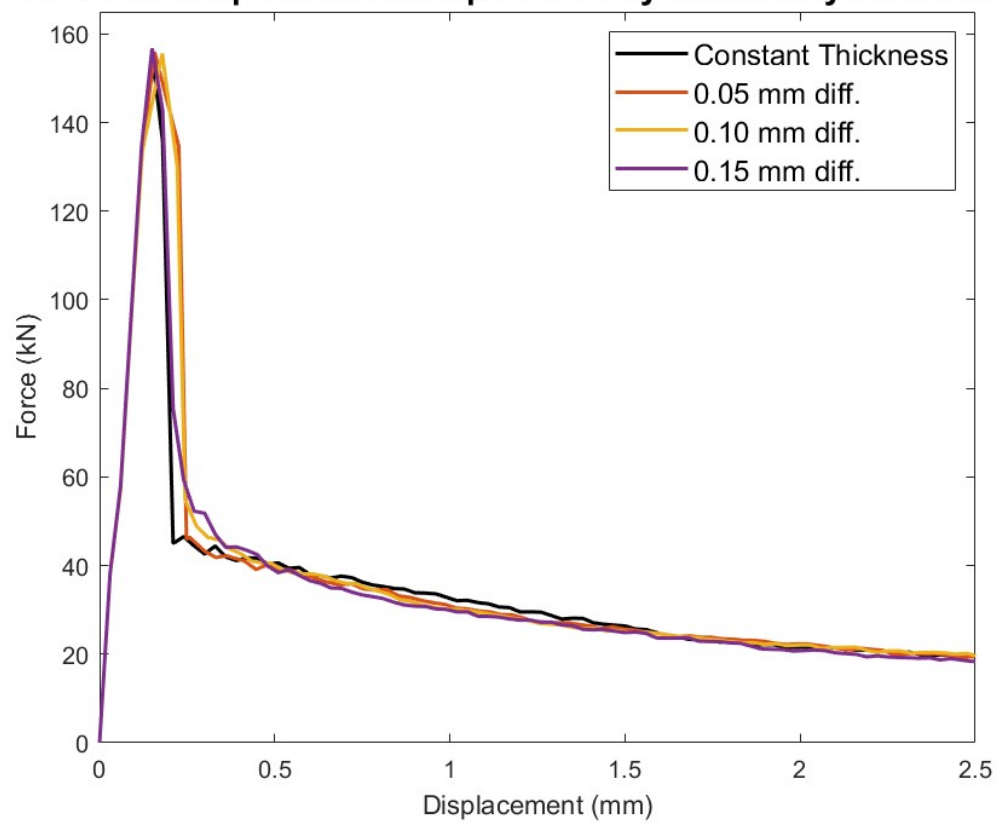


Figure 45. ANSYS-Derived Force-Displacement Graphs for 3 Layered Honeycomb Designs

FEA Force Displacement Graph for 5 Layered Honeycomb Designs

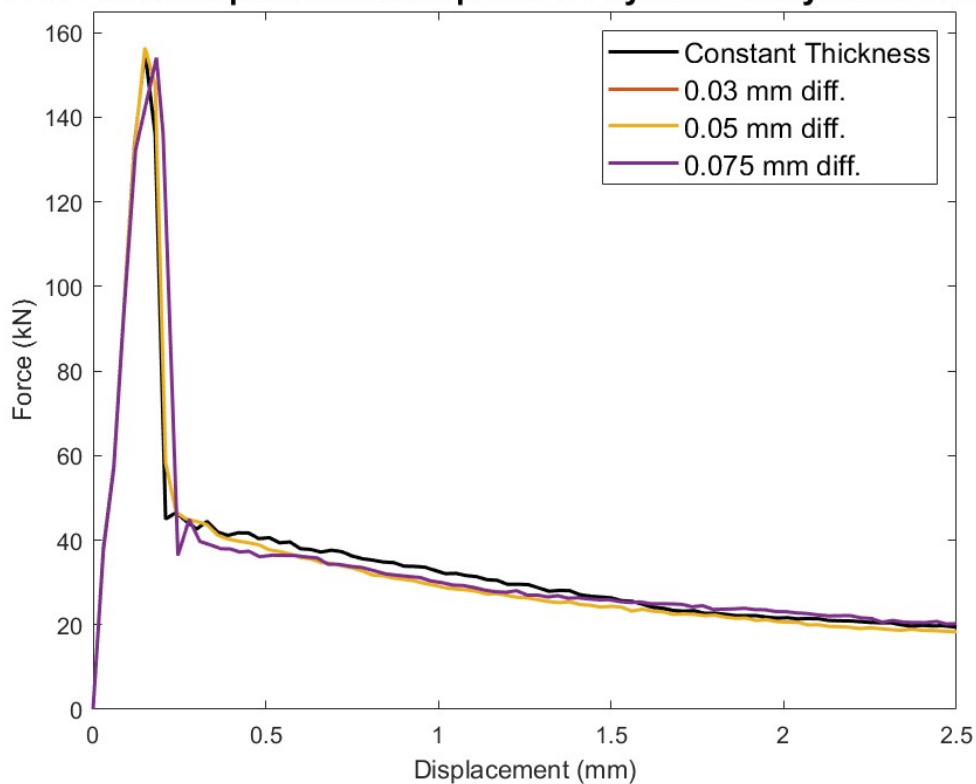


Figure 46. ANSYS-Derived Force-Displacement Graphs for 5 Layered Honeycomb Designs

Table 23. FEA Results for Modified Layered Honeycomb Designs

Simulation	Peak Force (KN)	Energy Absorbed in First 2.5mm (J)
Constant Thickness	155.580	86.143
3 Layered (0.05 mm layer diff.)	155.924	88.832
3 Layered (0.10 mm layer diff.)	155.588	88.603
3 Layered (0.15 mm layer diff.)	156.728	85.533
5 Layered (0.03 mm layer diff.)	154.052	85.920
5 Layered (0.05 mm layer diff.)	156.440	82.635
5 Layered (0.075 mm layer diff.)	154.052	85.92

7.4.3 Layered Honeycomb with Square and Enneagonal Tubes Results

Next, the modified layered honeycomb designs were simulated in enneagonal tubes which had demonstrated a higher peak force. From the results in Tables 23-24 and Figures 47-48 below, we observe that the results for enneagonal combinations have a much higher peak force and energy absorption compared with the square tube combinations. It is clear that there is not much difference in the peak force of each combination within the various layered combinations of square or enneagonal category. On the other hand, the energy absorbed indicates that some combinations may have better energy absorbing capabilities than others. This observation should be taken lightly due to the limitations of the elastic-perfectly plastic material model, especially after the yield point which is represented by the peak force on the force-displacement curve. As such, experimental testing of the designs would yield more concrete conclusions about the energy absorption of each combination.

Table 24. FEA Results for Square Tubes filled with Layered Tubes

<i>Simulation</i>	<i>Peak Force (KN)</i>	<i>Energy Absorbed in 35mm (J)</i>
Constant Thickness	238.972	1820.84
3 Layered (0.05 mm layer diff.)	238.784	1806.313
3 Layered (0.10 mm layer diff.)	239.176	1802.312
3 Layered (0.15 mm layer diff.)	239.368	1849.136
5 Layered (0.03 mm layer diff.)	237.532	1728.420
5 Layered (0.05 mm layer diff.)	237.460	1797.451
5 Layered (0.075 mm layer diff.)	238.288	1806.189

Table 25. FEA Results for Enneagonal Tubes filled with Layered Tubes

Simulation	Peak Force (kN)	Energy Absorbed in 35mm (J)
Constant Thickness	340.82	4668.023
3 Layered (0.05 mm layer diff.)	342.12	4814.78
3 Layered (0.10 mm layer diff.)	340.84	2422.65
3 Layered (0.15 mm layer diff.)	343.20	4796.82
5 Layered (0.03 mm layer diff.)	340.84	4596.47
5 Layered (0.05 mm layer diff.)	342.18	4717.93
5 Layered (0.075 mm layer diff.)	TBD	TBD

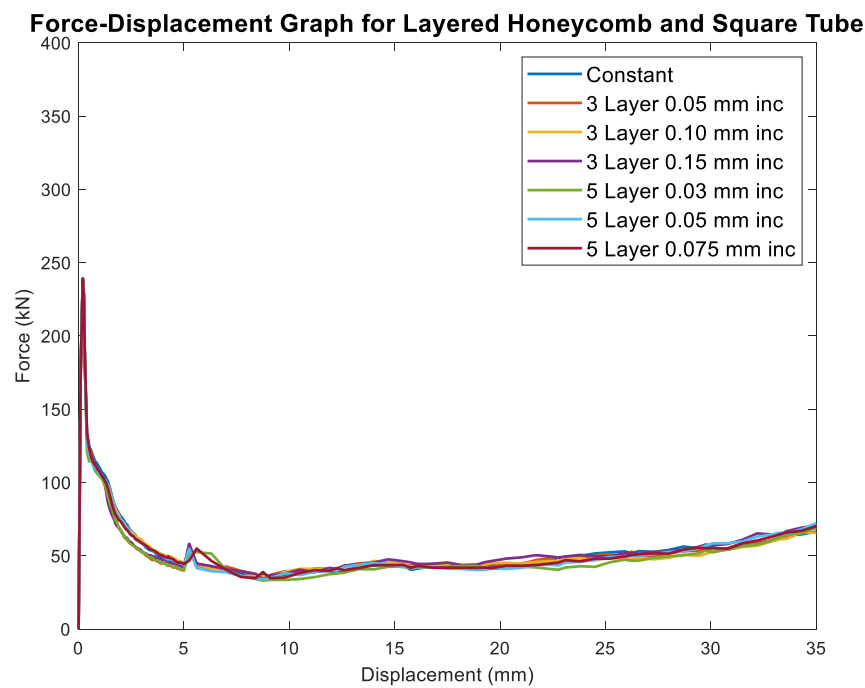


Figure 47. Force Displacement Curves for Square Tubes filled with Layered Tubes

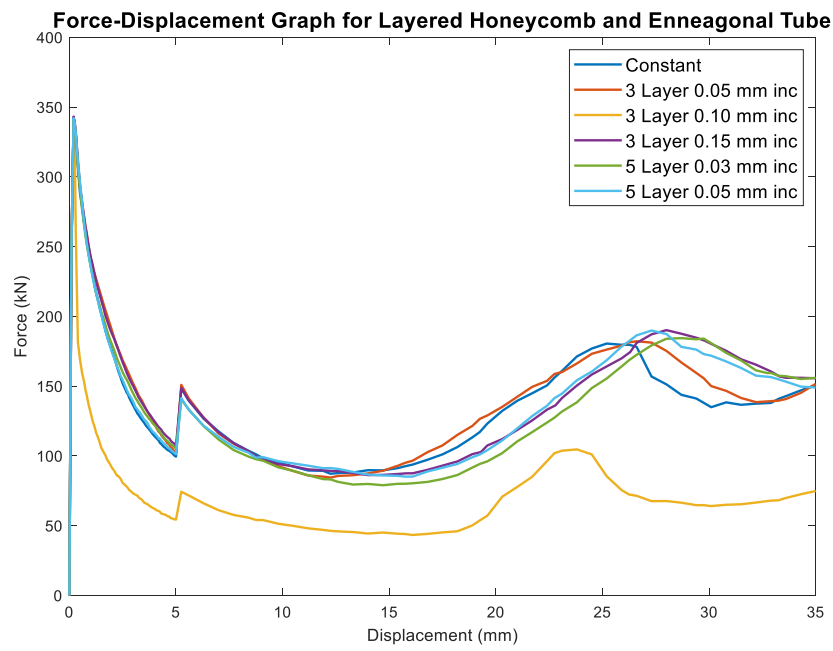


Figure 48. Force Displacement Curves for Enneagonal Tubes filled with Layered Tubes

7.4.4 Functionally Graded Honeycomb Results

As mentioned in Section 7-c, a 5mm x 5mm x 5mm functionally graded honeycomb was simulated instead of the full 50 mm x 50 mm x 50 mm to decrease computational expense. At least four solid elements were used through the thickness of each wall. To capture the peak crush force, the geometry was compressed 0.3 mm and the results are shown in Figure 49.

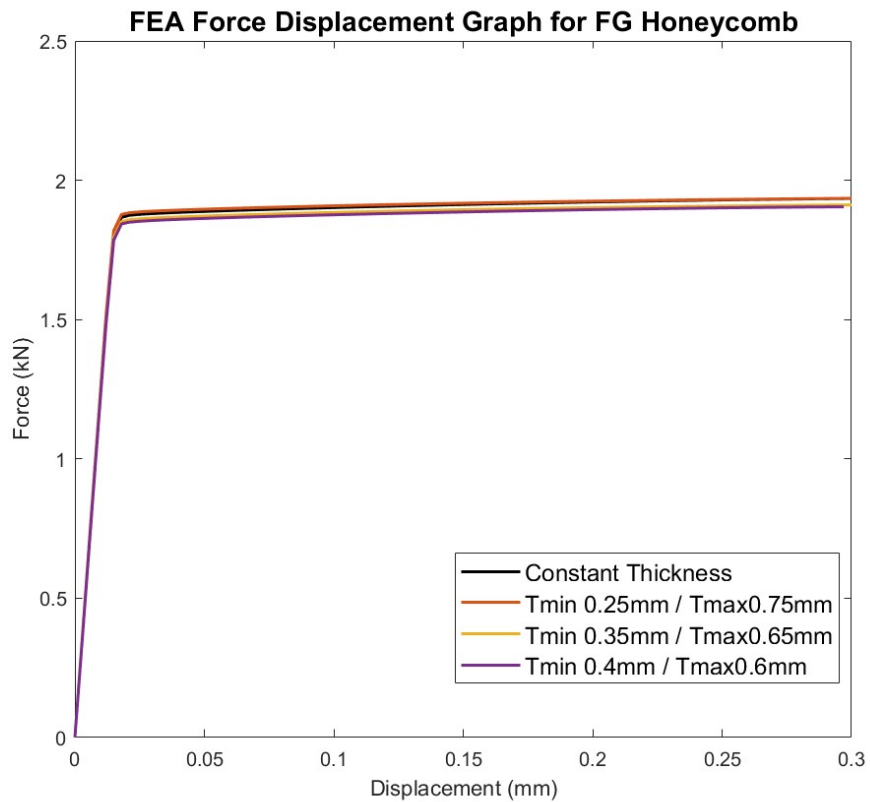


Figure 49. Force Displacement Curves for FG Honeycomb

As seen in Figure 49, according to FEA results, the influence of functionally grading the honeycomb cell wall thickness is minimal. While the FG honeycomb with the greatest difference between maximum thickness (0.75 mm) and minimum thickness (0.25 mm) yielded the greatest peak force, the improvement from the constant thickness run is almost negligible.

8 Ethics

Such a design will be beneficial for all of humanity due to the universal use of cars as a mode of transportation and the universal need for safe, environmentally friendly, and cost-effective cars. The intent of the design project is to investigate the crumple zone which is the major safety

component in vehicles. Thus, the ethical concern is significant since it involves human life not only in bodily safety, but also in the cost of having a safer and low-emission car. Thus, the design process is seriously carried out in its various steps, from literature review, verification and validation procedures, finite element analysis to 3D printing and experimental testing, before reaching the final design in order to reduce chances of error. Moreover, the codes and standards of the crumple zone performance, which are detailed in the [appendix](#), are followed throughout the design of the longitudinal beams.

The ethics surrounding the cost is also considered in the sense it would be unethical to promote a safe and more environmentally friendly design that is unattainable due to a high cost. Therefore, we aim to reduce the cost as much as possible by using lightweight but inexpensive materials.

The nature of the project as a final year undergraduate-level project limits the full-testing capabilities in full car collisions. Thus, the final design presented here will not be ready for use in cars before being tested thoroughly by the relevant authorities including car manufacturers and official certification bodies. Finite element modeling is performed on the longitudinal beam design, and the design will be 3D-printed and experimentally tested as a component, but it would not be integrated into the entire crumple zone or a full car.

9 Impact of Covid-19

COVID-19 had no notable impact on this capstone project.

10. Did the design meet the requirements?

10.1 Criteria for Testing

10.1.1 Peak Crush Force (PCF)

The peak crush force was used as a criteria for testing. Increasing PCF indicates that the longitudinal beams maximum force absorption increases; therefore, passengers experience a decreased force during the collision. Thus, it is a key metric in optimizing the performance of the longitudinal beam. When analyzing the performance of modified designs, the peak crush force should stay within similar magnitudes to the PCF of baseline designs: the square tube and constant thickness honeycomb.

10.1.2 Specific Energy Absorption (SEA)

Specific energy absorption was also used as a criteria for testing. Increasing SEA indicates an improvement in the compressive ability of the longitudinal beam and/or a decrease in the mass of the longitudinal beam. Thus, it is a key metric in determining the performance of the beam in accordance of this project's goals of decreasing CO₂ emissions and optimizing the crumple zone. However, for the ANSYS explicit dynamic simulations, findings regarding energy absorption will not be valued highly due to the inaccuracy of the material model after yielding. Instead, experimental compression tests will provide valuable results. Furthermore, in order to gauge the performance of the longitudinal beam outside of this study, findings will be compared with the required EA and SEA values for longitudinal

beams from the National Highway Traffic Safety Administration (NHTSA) as shown in Appendix 1.

10.2 Test Data

10.2.1 Geometries Printed

The seven geometries printed are listed below:

1. Constant thickness honeycomb-filled square tube
2. FG Honeycomb-Filled Square Tube ($T_{\min} = 0.3 \text{ mm}$ $T_{\max} = 0.7 \text{ mm}$)
3. FG Honeycomb-Filled Square Tube ($T_{\min} = 0.4 \text{ mm}$ $T_{\max} = 0.6 \text{ mm}$)
4. FG Honeycomb-Filled Enneagonal Tube (Optimal T_{\max} and T_{\min} Design)
5. 5 Layered Honeycomb-Filled Square Tube (0.03 mm Layer Increment)
6. 5 Layered Honeycomb-Filled Square Tube (0.075 mm Layer Increment)
7. 5 Layered Honeycomb-Filled Enneagonal Tube (Optimal Layer Increment)

EXPERIMENTAL TESTING WILL BE HERE

10.2.2 Discussion on the Testing Data

The peak crush force values of all modified designs were within the range of baseline designs according to FEA simulation. For instance, all 3-layered and 5-layered honeycombs had very similar PCFs to the constant honeycomb. However, these FEA simulations also showed little to no benefit in modifying the honeycomb to be either layered or FG. PCF differences between the different fillings in FEA simulation are negligible and energy absorption values are unreliable due to the material model. Thus, while the results for the modified honeycomb designs meet the testing criteria through their similar performance to their baseline counterparts, they do not pose any value for

implementation as it stands. However, it is possible that experimental results may yield different findings, so a holistic assessment of their performance will be done after experimental compression testing is completed. Nonetheless, enneagonal shaped tubes have proven to be optimal according to FEA simulation. With increased peak crush forces and large increases in SEA, enneagonal shaped tubes have proven to be a much better option in terms of crashworthiness than square tubes. As mentioned before, these energy absorption results from FEA will be validated with experimental testing.

11. Project Management

12. References

- [1] *Global status report on road safety 2018*. Geneva, Switzerland: World Health Organization, 2018.
- [2] *Global Road Safety Facility (GRSF) Annual Report 2021 (English)*. Washington, D.C. : World Bank Group.
<http://documents.worldbank.org/curated/en/251751646720074441/Global-Road-Safety-Facility-GRSF-Annual-Report-2021>
- [3] "CO₂ emission performance standards for cars and Vans," *Climate Action*. [Online]. Available: https://climate.ec.europa.eu/eu-action/transport-emissions/road-transport-reducing-co2-emissions-vehicles/co2-emission-performance-standards-cars-and-vans_en. [Accessed: 04-Nov-2022].
- [4] D.Vangi, *Vehicle collision dynamics: Analysis and reconstruction*. Oxford: Butterworth-Heinemann, 2020.
- [5] Fang, Jianguang, et al. "On design optimization for structural crashworthiness and its state of the art." *Structural and Multidisciplinary Optimization* 55.3 (2017): 1091-1119.
- [6] Abdulqadir, Samer Fakhri. "Design a new energy absorber longitudinal member and compare with S-shaped design to enhance the energy absorption capability." *Alexandria engineering journal* 57.4 (2018): 3405-3418.
- [7] H. Singh (2022). "Structural Design Considerations for a Lightweight Vehicle to Achieve "Good" Rating in IIHS Small Overlap" [PowerPoint slides]. Available:
https://www.safercar.gov/sites/iihs.safercar.gov/files/2015sae-singh-structuredesign-iihs_sol.pdf
- [8] Wiacek, Christopher, et al. "Evaluation of frontal crash stiffness measures from the US New car assessment program." *ESV Conference, Seoul, South Korea*. 2015.

- [9] R. D. Hussein, D. Ruan, G. Lu, S. Guillow, and J. W. Yoon, "Crushing response of square aluminium tubes filled with polyurethane foam and aluminium honeycomb," *Thin-Walled Structures*, 10-Nov-2016. [Online]. Available:
- [10] Koora, Ramesh, Ramavath Suman, and Syed Azam Pasha Quadri. "Design Optimization of Crush Beams of SUV Chassis for Crashworthiness." *International. Jounal. of Science and Research* 5 (2016)
- [11] R. Qin, J. Zhou, and B. Chen, "Crashworthiness design and multiobjective optimization for hexagon honeycomb structure with functionally graded thickness," *Advances in Materials Science and Engineering*, 06-Feb-2019. [Online]. Available: <https://www.hindawi.com/journals/amse/2019/8938696/#B10>. [Accessed: 04-Nov-2022].
- [12] H. Yin, G. Wen, S. Hou, and K. Chen, "Crushing analysis and multiobjective crashworthiness optimization of honeycomb-filled single and bitubular polygonal tubes," *Materials & Design*, vol. 32, no. 8-9, pp. 4449–4460, Sep. 2011.
- [13] "Material Specifications - 6060 T5 Aluminium Alloy | Fabrication Services | Welding | Caloundra | APAC," Apacinfrastructure.com.au, 2022.
<https://apacinfrastructure.com.au/material-specifications-6060-t5-aluminium-alloy>.
- [14] "5052-H39 Aluminum :: MakeItFrom.com," Makeitfrom.com, May 30, 2020.
<https://www.makeitfrom.com/material-properties/5052-H39-Aluminum>.
- [15] "Aluminum 5052-H38," Matweb.com, 2022.
<https://www.matweb.com/search/datasheet.aspx?MatGUID=03ed379e437945a1a8dbff86c5907f74&ckck=1>.

- [16] “Engineering at Alberta Courses» Plasticity in Uniaxial Stress State,” *Engcourses-uofa.ca*, 2022. <https://engcourses-uofa.ca/books/introduction-to-solid-mechanics/constitutive-laws/plasticity/mathematical-modelling-of-plasticity/plasticity-in-uniaxial-stress-state/>.
- [17] “Al-alloy AISI10MG - SLM solutions,” *Al-Alloy AISI10MG Data Sheet*. [Online]. Available: https://www.slm-solutions.com/fileadmin/Content/Powder/MDS/MDS_Al-Alloy_AISI10Mg_0520_EN.pdf. [Accessed: 25-Mar-2023].
- [18] L. Hitzler, N. Schoch, B. Heine, M. Merkel, W. Hall, and A. Öchsner, “Compressive behaviour of additively manufactured alsi10mg,” *Materialwissenschaft und Werkstofftechnik*, vol. 49, no. 5, pp. 683–688, May 2018.
- [19] E. Sert, E. Schuch, A. Öchsner, L. Hitzler, E. Werner, and M. Merkel, “Tensile strength performance with determination of the Poisson’s ratio of additively manufactured alsi10mg samples,” *Materialwissenschaft und Werkstofftechnik*, vol. 50, no. 5, pp. 539–545, May 2019.

13. Appendix

Appendix 1: Required EA and SEA Values for Conventional Car Longitudinal Beams [6]

Test	EA (kJ)	SEA (kJ/kg)
Full overlap (NHTSA)	30	6
40% overlap (IIHS)	20	4
Oblique Loading (30 degrees)	11.5	2.4

Appendix 2: Allowable Displacement of Car Parts according to their Grade and Location [7]

	Measured Intrusion into Passenger Box (cm)	
	Lower Occupant Compartment	Upper Occupant Compartment
Good	0 - 15	0 - 7.5
Acceptable	15 - 22.5	7.5 - 12.5
Marginal	22.5 - 30	12.5 - 17.5
Poor	> 30	> 17.5

Appendix 3: Reference Stiffness Values for Crumple Zones Based on 2002-2014 Vehicle Models’ Averages [8]

<i>Type of stiffness value</i>	<i>Value for Multi-Purpose Vehicles (N/mm)</i>	<i>Value for Passenger Cars (N/mm)</i>	<i>Value for Light Duty Pickup Trucks (N/mm)</i>
Linear “Initial” Stiffness	1895	1336	2448
Energy-Equivalent Stiffness	1502	1171	1720
Static Stiffness	2160	1913	2149
Dynamic Stiffness	1191	959	1409